Analysis of the unstable behavior of a pump-turbine in turbine mode: fluid-dynamical and spectral characterization of the S-Shape characteristic

Giovanna Cavazzini[1]
Department of Industrial Engineering, University of Padova
Via Venezia 1, 35131, Padova, Italy
Giovanna.cavazzini@unipd.it

Alberto Covi
Department of Industrial Engineering, University of Padova
Via Venezia 1, 35131, Padova, Italy
Alberto.covi@unipd.it

Giorgio Pavesi
Department of Industrial Engineering, University of Padova
Via Venezia 1, 35131, Padova, Italy
Giorgio.pavesi@unipd.it

Guido Ardizzon
Department of Industrial Engineering, University of Padova
Via Venezia 1, 35131, Padova, Italy
guido.ardizzon@unipd.it

ABSTRACT

The most common mechanical equipment adopted in the new generation of pumped-hydro power plants

is represented by reversible pump-turbines, required to rapidly switch between pumping and generating

modes in order to balance the frequent changes in electricity production and consumption caused by

unpredictable renewable energy sources. As a consequence, pump-turbines are required to extend their

operation under off-design conditions in unstable operating areas.

---

[1] Tel. +39-049-8276800

The paper presents a numerical analysis of the unstable behavior of a pump-turbine operating in turbine mode near the no-load condition. To study in depth the unsteady phenomena which lead to the S-shape of the turbine characteristic, a load rejection scenario at constant and large guide vane opening was numerically analyzed by running through the flow-speed characteristic up to the turbine brake region. The flow field analysis led to the onset and development of unsteady phenomena progressively evolving in an organized rotating stall (65.1% of the runner rotation frequency) during the turbine brake operation. These phenomena were characterized by frequency and time-frequency analyses of several numerical signals (static pressure, blade torque, mass flow rate in blade passages).

The influence of the development of these unsteady phenomena on the pump-turbine performance in a turbine operation was also analyzed, and the potential causes that generated the S-Shaped characteristic curve were also investigated.

1. INTRODUCTION

Storing electrical energy is a key issue when it comes to significantly increasing the exploitation of unpredictable renewable energy sources, such as wind and solar energy sources.

Today, one of the most promising and tested ways of storing electricity is undoubtedly pumped hydro energy storage which is characterized by high efficiency ranges (75-85%), competitive costs (600-1000 €/kW) [1] and good connection properties (good reaction time from pumping mode to turbine mode) [2].

The most common mechanical equipment adopted in the new generation of pumped-hydro energy plants is represented by reversible pump-turbines (RPT), generally preferred to other technical arrangements due to their cost-effectiveness.

To balance the frequent changes in electricity production and consumption caused by a large share of unpredictable renewable energy sources, pump-turbines are required to rapidly switch between pumping and generating modes, extending their operation under off-design conditions. In particular, in generation mode, during the start-up procedure, the machine is put in no-load operation (runaway operation) and to be coupled with the grid, its rotation frequency should be synchronized with the grid frequency level. Since the accepted frequency oscillation amplitudes are very small (generally ± 0.4%), under these working conditions the pump-turbine should operate at a stable state of operation, that is without significant speed oscillations.

However, the design of a pump-turbine is the result of a compromise between opposing targets, namely pump and turbine performance, regulation capacity, efficiency and cavitation behaviour. The design criterion mainly focuses on the pump behaviour due to greater sensitivity of the pumping flow field to boundary layer detachments and flow separations. This design criterion may induce an unstable Q_{ED}-n_{ED} (fig. 1) characteristic curve in turbine operation mode represented by a typical S-shaped profile with a positive slope in the turbine brake operation.

As a consequence of this positive slope, close to the runaway condition the pump-turbine may switch forth and back from generating to reverse pumping mode, causing severe torque fluctuations as well as significant fluctuations of the head and flow rate with possible self-excited vibrations [3,4] or water hammers. Such a phenomenon could stress not only the mechanical equipment, but the entire power plant [5]. This unstable behavior leads to speed instability both during the start-up

sequence, slowing down or preventing the start-up process, and during the turbine

brake, especially in the case of load rejection before the pump-turbine switches off.

It has been observed that the appearance of these system instabilities and

oscillations is strictly related to the design criteria of the pump-turbine, since they do

not affect the performance of the Francis turbines under the same operating conditions

[6]. Moreover, a necessary but not sufficient condition for the occurrence of this

unstable behavior has been identified in the negative slope of the head curve (dH/dQ<0)

[7].

As regards the reasons for this S-shaped characteristic, these seem to be related

to the development in the pump-turbine of vortexes partially blocking the flow [8-10] or

of stall cells rotating in the runner channels at 50-70% of the runner rotation frequency

[11-13]. To study more in depth the characteristics of this rotating stall, the load

rejection of a pump-turbine was numerically analysed by Widmer et al. [14] whose

analysis mainly focused on the evolution in time of these unsteady phenomena in the

guide vanes.

To detect the development of a rotating stall in pump-turbine, Botero et al. [15]

recently proposed an interesting non-intrusive diagnostic method based on the cyclic-

frequency analysis of the guide-vane vibrations.

However, to the authors' knowledge, the causes of the S-shape appearance in

the performance curves are still not completely clear, so no innovative design criteria

have been proposed to overcome the limits in the stable operating range deriving from

this type of characteristic curve. Only few attempts aimed at identifying geometry

modifications which bring about improvements to the pump-turbine stable behaviour were presented by Gentner et al. [4], Olimstad et al. [6], Houdeline et al. [16] and Yin et al. [17].

The aim of this paper is to investigate thoroughly the onset and the development of these unsteady phenomena in the pump-turbine and to correlate the intensity and characteristics of the identified instability with the appearance of the S-shape in the speed-discharge curve.

The paper is organized as follows: in section 2 the numerical model of the RPT is presented; section 3 reports the results of the model validation by comparing them with experimental results in stable operating conditions; section 4 presents the results of the fluid-dynamical and spectral characterization of the unsteady phenomena leading to the unstable behaviour; in section 5 the effects of the unstable behavior on the pump-turbine performance curve are presented together with an explanation of the fluid-dynamical reasons of the appearance of the S-shape in the speed-discharge curve.

2. THE NUMERICAL MODEL

Numerical analyses were carried out using the commercial software ANSYS 14.5 on the first stage of a two stage reversible pump-turbine in turbine-operating mode (fig. 2).

The scaled down model consists of a radial, shrouded impeller with 7 three-dimensional backward swept blades with a design specific speed n_s=37.6 $m^{0.75}s^{-1}$ (dimensionless design specific speed ω_s=0.71). Twenty-two adjustable guide vanes are

coupled with 11 continuous vanes. The guide vane angles and their relative azimuthal position with the return channel vanes are continuously and independently adjustable to analyze the influence of the relative position on the pump-turbine behavior. Table 1 reports the main geometrical data of the considered pump-turbine, whereas the references of the main diameters are reported in fig. 3.

In the analyzed configuration, the radial gap between the trailing edge of the guide vanes and the runner tip was 10.5 mm, which is 5.25% of the impeller radius. The relative azimuthal position of the guide vanes was fixed by rotating the whole guide vane system from the face-to-face configuration ($\lambda=0°$ - fig. 4) to the configuration with the azimuthal position of the guide vanes +8° out of alignment. Since the study was aimed at reproducing the load rejection scenario of a pump-turbine, a large guide vane opening (GVO) of 18°, also presenting an unstable behavior in pumping mode [18], was considered.

The numerical model of the entire machine included inlet duct, return channel, guide vanes (distributor), runner, draft tube and leakage system. fig. 5 reports the meridional plot of the model.

The draft tube was discretized by a structured mesh of about 322,400 elements with a y+ value no greater than 30 for the elements closest to the wall. As regards the runner, an O grid was adopted. The stage head H and the stage efficiency were evaluated in preliminary tests to ensure a grid independent solution for the runner and to guarantee the capacity of the numerical solution to capture the local pressure pulsations as well.

The resulting computational domain of the runner used had a total of 3.7 million cells with y+ values below 30. O-type grids were adopted for both the distributor and the return channel discretization with about 3.55 and 5.11 million cells, respectively. To take into account the influence of the leakage flow rate on the flow field evolution at part loads, the labyrinth seal was also modeled by means of several H-blocks. Table 2 summarizes the main data of the resulting fully hexahedral mesh, whereas fig. 6 reports a detail of the meshed domains.

The choice of the turbulence model is a key issue in CFD. According to the large flow separations expected in the unstable operating range, a detached eddy simulation (DES) model was adopted. The shear stress transport k-omega model covered the boundary layer while the Smagorinsky-Lilly model was applied in detached regions. On both blades and wall surfaces, the boundary layer was assumed to be fully turbulent. All the interfaces between stator-rotor blocks were standard transient sliding interfaces.

The mass flow with stochastic fluctuations of the velocities with a 5% free stream turbulent intensity was imposed at the inlet boundary condition (BC), the mass flow value being taken from the experimentally investigated operating point. At the outlet BC, due to the highly disturbed flow field, an opening condition with an average static pressure (relative pressure equals to 0 Pa) was fixed. Walls are defined with no-slip wall BCs. Runner blades, runner hub and shroud, walls of the leakage system belonging to the runner and shaft wall were fixed as rotating walls.

A second-order implicit time-stepping was adopted for the time discretization and a time step of 1° with a maximum number of coefficient loops (i.e. number of iterations per time step) equal to 6 was defined.

The maximum Courant number resulted to be lower than 3 for all the analyzed flow rates, guaranteeing an accurate resolution of the transient details. The resulting RMS values for the residuals were: u momentum 10^{-5}, v momentum 10^{-5}, w momentum 10^{-6}, and turbulence kinetic energy 10^{-5}.

3. VALIDATION OF THE NUMERICAL MODEL IN STABLE OPERATING CONDITIONS

To validate the numerical model, the numerical performance curves were compared with those experimentally acquired on the first stage of the RPT according to ISO standards (fig. 7).

Numerical analyses have been carried out for 5 operating points (59.1%Q_{bep}, 65.5%Q_{bep}, 77.4%Q_{bep}, Q_{bep}, 108.5%Q_{bep}) at a constant rotation rate of 600 rpm and the comparison in terms of head, power and efficiency is reported in fig. 8. The Reynolds number was equal to $5.63*10^6$.

The agreement between numerical and experimental results are quite good in terms of head, with an error smaller than 5% near the best efficiency point and smaller than about 7.5% at partial loads (fig. 9). As regards the mechanical power, near the best efficiency point the percentage errors are still smaller than 5% with a numerical overestimation that seems to be mainly due to the mechanical friction losses, not considered in the numerical model. Since these losses are strictly related to the runner rotation rate, they are expected not to significantly vary at partial loads, as verified by

the absolute errors in power nearly constant in all the operating conditions. The

corresponding reduction of the mechanical power at partial loads justifies the significant

increase in percentage errors at partial loads (38% of power error for 59.1%Q_{bep}).

At partial loads, the overestimation of the mechanical power, combined with the

overestimation of the head, results in an overestimation of the efficiency (29.74% of

error for 59.1%Q_{bep}). On the other side, close to the best efficiency point, the

overestimation of the head is slightly greater than the overestimation of the mechanical

power, resulting in a small underestimation of the efficiency (smaller than 2% for Q_{bep}).

So, in spite of the simplification related to the mechanical friction losses, the

good agreement in terms of trends and errors between numerical and experimental

results demonstrated the capability of the numerical model to predict the performance

of the pump-turbine with sufficient accuracy.

It must be pointed out that, due to the overestimation of the mechanical power,

the no-load condition is numerically reached at a lower flow rate than the experimental

one. However, since the mechanical friction losses do not affect the flow field evolution,

a negligible influence on the spectral and fluid-dynamical characterization of the

unsteady phenomena can be assumed.

4. NUMERICAL ANALYSIS OF THE PUMP-TURBINE BEHAVIOUR IN A LOAD REJECTION SCENARIO

4.1 Numerical simulation

In order to study the evolution of the flow field in an unstable operating area, a

load rejection scenario with servomotor failure was reproduced. Since such a scenario

refers to medium to large guide vane openings, the GVO was fixed at 18° and kept constant during the simulation.

From a numerical point of view, it was hence necessary to carry out a transient numerical simulation on the entire machine with a time-varying boundary condition in which the mass flow rate at the inlet was slightly reduced every time step so as to run through the characteristic curve. In this case a simple linear variation of the mass flow rate from 45.1% to 15.9% $Q_{m,bep}$ in about 20 runner revolutions, was chosen according to the following equation:

$$Q_m(t) = 45.1\% Q_{bep} * \rho - K * t \qquad (1)$$

The simulation started at Q/Q_{bep} =45.1% (P=0.34 kW; η=0.18), slightly above the runaway condition (Q/Q_{bep} =37.6%; P=6*10^{-4} kW; η=0.04) where the unstable phenomena was expected to start to develop (fig. 10). The initialization was based on the results of the steady simulation carried out for the same mass flow rate.

The rotational speed (600 rpm) remained constant during the simulation and twenty complete runner revolutions were simulated to investigate the whole operating range affected by the development of the rotating stall.

Since the simulation of the turbine brake was rather CPU-time consuming, the number of coefficient loops for each time step was reduced to 3, with a time step still equal to 1° of runner rotation.

Even though this modification slightly increased the simulation residuals (u momentum= 10^{-4}, v momentum=10^{-4}, w momentum=10^{-5}, turbulence kinetic energy=10^{-4}), the resulting performance of the pump-turbine resulted not to be affected.

4.2 Analysis of the flow field evolution in a load rejection scenario

Fig. 11 reports the flow pattern in the unstable branch of the characteristic curve (21.8% Q_{bep} – t_3 in fig. 10) in the runner (relative streamlines) and in the distributor (absolute streamlines). As it can be seen, the flow field is extremely perturbed with the development of medium to large vortexes partially or totally blocking the channels in both the runner and the distributor. To analyse the reason of the development of these flow structures, the instantaneous velocity fields at mid-span inside the runner and guide vanes were compared for three different instants corresponding to three different flow rates (fig. 10): t_1) 45.1%Q_{bep}, t_2) 37.8%Q_{bep} and t_3) 21.8%Q_{bep}.

Fig. 12a represents the velocity field at the beginning of the simulation (45.1%Q_{bep}). It is clear that the onset of flow detachments (A in fig. 12a) on the blade pressure side (PS) starts to perturb the flow field slightly in the first half of the runner channels. During the turbine brake, the progressive reduction of the mass flow rate causes the development and enlargement of these regions of flow separation, with the onset of a back flow near the inlet throat of some channels (B in fig. 12b). Further reductions of the inlet mass flow rate leads to the full blockage of the flow in some runner channels as a consequence of large vortexes developing across the whole passage section (C in fig. 12c). Since guide vanes are very close to the runner, flow field development in the distributor is affected by the unsteady phenomena developing in the runner and, consequently, the distributor blades were also alternately blocked or stalled (D in fig. 12c).

The blockage action is confirmed by the analysis of the flow rate passing through the channels of the runner and guide vanes. Fig. 13 reports the contour plot of the difference in percentage between the instantaneous flow rate $q_{i,Q}$ passing through the channel i and the theoretical mean value ($\sum_{i=1}^{n_b} q_{i,Q}/n_b$):

$$\varepsilon_i = \frac{q_{i,Q} - \frac{1}{n_b}\sum_{i=1}^{n_b} q_{i,Q}}{\frac{1}{n_b}\sum_{i=1}^{n_b} q_{i,Q}} \quad (i = 1..n_b) \tag{2}$$

where Q is the instantaneous flow rate passing through the machine at that instant and n_b is the number of runner blades (fig. 13a) or guide vanes (fig. 13b) . The reference surfaces inside the runner and the distributor on which the mass flow rates $q_{i,Q}$ have been evaluated are reported in fig. 3.

Fig. 13 shows how, during load rejection, several channels in the pump-turbine were blocked (ε_i=-1; $q_{i,Q}$ =0) or characterized by a back flow (ε_i<-1; $q_{i,Q}$ <0).

As regards the runner (fig. 13a) the channels start to be blocked from nearly 24.5% Q_{bep}. The stall cell, partially or fully blocking the regular flow, moves from one channel to the subsequent one against the runner rotation direction with increasing intensity during the load rejection. Each runner channel alternates between sound flow, blocked flow and back flow, according to the rotation frequency of the stall cell.

In the guide vanes, the flow field is perturbed by a sort of unsteady stall phenomena from the very beginning of the simulation with channels characterized by sound flow, blocked flow or back flow. However, it is only when an organized rotating structure appears in the runner (Q/Q_{bep}=24.5%) that these unsteady phenomena evolved towards a stable rotating stall, whose intensity is even stronger than it is in the

runner (Fig. 13b). Here, the blocking effect, affecting simultaneously more channels

moves according to the runner rotation direction from one channel to the next.

The development of these unsteady phenomena in the runner obviously

affected the pressure distribution on the runner blades, thereby modifying their load

distribution.

Fig. 14 reports the instantaneous pressure distribution on a runner blade (blade

2 in fig. 12), located in the perturbed area with increasing intensity of stall phenomena.

The same three instants of fig. 12 have been considered:t_1 – Q= 45.1%Q_{bep}; t_2 –

Q=37.8%Q_{bep}; t_3 – Q=21.8%Q_{bep}.

Close to the runaway condition, the flow around blade 2 is perturbed in the very

first part of the blade by the onset of flow detachments, whereas the remaining part of

the blade is working properly (fig. 14a). When the mass flow rate is further reduced and

the runner operates below the runaway condition (fig. 14b), almost half of the blade is

affected by the unsteady phenomena and the pressure on the suction side (SS) is quite

close to that on the pressure side: the blade is stalling (T=0.9 Nm). For smaller mass flow

rates (fig. 14c), the channel near blade 2 is completely blocked by a stall cell (fig. 12c)

and the pressure on the pressure side (PS) becomes smaller than on the suction side

(SS), resulting in a negative torque: the blade behaved like a pump blade (reverse

pump).

Due to the rotating characteristics of these stall cells, the blades are

characterized by time fluctuations of the pressure distributions and hence of the torque,

depending on the evolution of the flow field around the blade. Fig. 15 reports the

evolution of the torque over time on three runner blades and four guide vanes during load rejection. Here, it is clear that the blades are subjected to continuous changes in blade operating mode: from turbine (positive blade torque) to reverse pump (negative blade torque) and vice-versa. For example, blade 2 at the instant t_3 (Q=21.8%Q_{bep}) is characterized by a negative torque (T=-7.6 Nm) and negative instantaneous flow rate ($q_{i,Q}$ =-0.24 l/s) that becomes positive (T=6.5 Nm and $q_{i,Q}$ =3.42 l/s) a few instants later (Q=20.3%Q_{bep}) as a consequence of the displacement of the stall cell in other channels (fig. 16). At this instant the blockage action is mainly affecting blade 4, as testified by the extremely negative torque (T=-10 Nm –fig. 15).

It is interesting to notice that the torque fluctuations on the runner blades increase in amplitude together with the intensity of the unsteady phenomena, with possible negative consequences on the fatigue resistance of the mechanical components.

4.3 Time-frequency characterization of the unstable behavior

A spectral analysis in frequency and in time-frequency domain was carried out to characterize the unsteady phenomena identified in the previous flow field analysis. More details about this type of spectral analysis can be found in Pavesi et al. [19].

Fig. 17 reports a scheme of the positions of some of the acquired numerical signals: static pressure signals (black and grey circles) acquired at the guide vanes inlet ($p^{4,1}$… $p^{4,7}$) and outlet ($p^{3,1}$ … $p^{3,7}$); torques acting on 7 guide vanes (highlighted with solid black lines) and on all the runner blades; mass flow rates passing through 7 guide vanes channels and all the runner channels.

The data were acquired simultaneously at a frequency of 3600 Hz (time step of 1° with a runner rotation rate of 600 rpm) during the whole simulation of load rejection. Due to the time-varying boundary conditions, the series of 7138 samples acquired during load rejection were not divided into overlapping segments for the spectral analysis, resulting in a frequency resolution of 0.50 Hz. The Hanning windowing function was chosen to avoid leakage errors in the spectral analysis.

To analyse the frequency content of the acquired numerical signals, the auto-spectra were determined according to the following equation:

$$G^{xx}(f) = \frac{1}{W_H}[X(f)X^*(f)]$$
(3)

where $X(f)$ and $X^*(f)$ are the fast Fourier transforms (FFT) and its complex conjugate of the signal x (torque, pressure or mass flow rate) respectively and W_H is the Hanning windowing function.

Fig. 18 reports the auto-spectra of the signals (mass flow rate and torque) acquired in the runner (rotating reference frame), whereas figs. 19 and 20 report the auto-spectra of the signals (mass flow rate, torque and static pressure) acquired in the guide vanes (stationary frame).

The auto-spectra of the runner signals (fig. 18) were dominated by a peak at $St_{RS,rot}$=0.051, whose amplitude is greater than that of the blade passage frequency ($St_{BPF,rot}$=3.142 in the rotating frame). The BPF is weakly appearing in the spectrum of the torque because it is due to the reflection action made by the stator parts, also perturbed by the development of the unsteady phenomena (fig. 18b).

As expected, the blade passage frequency is much more pronounced in the auto-spectra of the distributor signals ($St_{BPF,st}$=1.0 in figs. 19 and 20), where a significant peak also appears at $St_{RS,st}$=0.093 (65.1% of the runner rotation frequency). This peak can be strictly related to the peak previously identified in the rotating frame ($St_{RS,rot}$) by means of the runner rotation frequency (St_{rr}=0.144), according to the following relation [20,21]:

$$St_{RS,rot} = St_{RS,st} - St_{rr} = -0.051$$

(4)

The negative value obtained for $St_{RS,rot}$ means that in the rotation reference frame the disturbance moves with a sub-synchronous frequency inside the runner against the rotation direction of the runner itself, whereas in the stationary frame it moves in the same direction. These results are in fully agreement with the evolution of the blockage action in the runner and guide vane channels (fig. 13).

It is also interesting to notice that at the guide vane outlet, due to the proximity of the runner inlet, the pressure pulsations, caused by the rotation of the runner blades, are strongly perceived by the guide vanes, dominating the resulting power spectrum (fig. 20a).

To verify the correlation between the different acquired signals and hence the existence of a single unsteady structure involving the whole runner, the cross spectra between two numerical signals have been also evaluated, according to the following equation:

$$G^{xy}(f) = \frac{1}{W_H}[Y(f)X^*(f)]$$

(5)

where $Y(f)$ and $X^*(f)$ are the FFTs of two different signals.

Fig. 21 reports some representative cross-spectra between mass flow rate and torque signals acquired in different runner positions. As can be seen, all the cross-spectra exhibit the previously identified peak at $St_{RS,rot}$, confirming the fact that the identified instability is an organized structure rotating inside the runner.

This result was also confirmed by the cross-spectra of the numerical signals (static pressure, torque and mass flow rates) acquired in the stationary reference frame (figs. 22 and 23) exhibiting a peak at $St_{RS,st}$.

This peak at $St_{RS,st}$ has the same amplitude of the blade passage frequency ($St_{BPF,st}$) in all the cross-spectra with the exception of the guide vane outlet. At this location, the pressure pulsations, caused by the rotation of the runner blades, are strongly perceived by the guide vanes (fig. 20a) and present an intense and obvious correlation between the different blades.

The signal processing in the frequency domain makes it possible to analyze the spectral components contained in a signal, but it does not make assigning these spectral components to time feasible. In order to identify the instant and hence the operating condition in which the frequency characterizing the rotating stall appears, a time-frequency characterization was performed via wavelet transform analysis.

For all the series of data the continuous wavelet transform W(s,n) was computed via the FFT-based fast convolution according to the following equation:

$$W(s,n^*) = \sum_{k=0}^{N-1} X_k \left(\sqrt{\frac{2\pi s}{\delta t}}\, \psi_0^*(s\omega_k)e^{i\omega_k n^* \delta t} \right)$$

(6)

where X_k is the DFT (discrete Fourier transform) of the discrete sampled signal x_n,

k is a frequency index, N is the length of the data series, s is the wavelet scale, δt is the

sampling interval, n^* is the localized time index. $\Psi^*_0(s\omega_k)$ is the complex conjugate of the

Fourier transform of the scaled version of the "mother wavelet" ψ(t) and ω_k is the

angular frequency (note that if $k \leq N/2$, $\omega_k=2\pi k/N\delta t$; else $\omega_k=-2\pi k/N\delta t$). The

normalization factor $\sqrt{2\pi s/\delta t}$ was introduced to obtain a unit energy at each scale. As

regards the choice of the mother wavelet, in this case, a complex Morlet wavelet with

$2\pi f_0=8$ was chosen [22].

Because of the finite-length time of the considered signals, errors occur at the

beginning and end of the wavelet power spectrum. The "cone of influence" (COI) is the

region of the wavelet spectrum in which edge effects become important and is

delimited with a broken line in figs. 24-26.

Fig. 24 reports the continuous wavelet transform of the signals of the mass flow

rate passing through the runner channel 2 (fig. 24a) and of the torque acting on the

runner blade 2 (fig. 24b).

Here in the runner, the frequency corresponding to the rotating stall ($St_{RS,rot}$) is

clearly identified and starts to appear from nearly 24.5% Q_{bep}. This result is also

confirmed by the continuous wavelet transforms calculated for the signals acquired in

the stator domain, some of which are reported in figs. 25 and 26.

As expected, the blade passage frequency is captured, with more or less

intensity during the whole load rejection simulation, in the wavelet transforms of the

signals of the torque acting on the guide vanes (fig. 25b) and of the static pressure at the guide vanes inlet and outlet (fig. 26).

The spectral characterization in the time-frequency domain demonstrates a relationship between the appearance of a well-defined frequency in the spectral content of the machine and the fluid-dynamical evolution of the unsteady phenomena during load rejection. It is only from 24.5%Q_{bep} that the perturbation of the pump-turbine flow field evolves in an organized rotating stall and, as it will be seen in the next chapter, this is the cause of the change in slope of the dimensionless discharge-speed curve and hence of its modification in an S-shaped curve.

5. INFLUENCE OF THE UNSTABLE BEHAVIOUR ON THE PUMP-TURBINE PERFORMANCE

Fig. 27 reports the head and mechanical power of the pump-turbine in the stable operating region (dots representing time-averaged performance values) and their evolution during load rejection (continuous lines). The development of the unsteady phenomena affects the pump-turbine performance, determining an increase in amplitude of the head oscillations. However, it is interesting to note that the head of the pump-turbine (fig. 27a) has a negative slope only for mass flow rates lower than 24.5%Q_{bep}, that is when the unsteady phenomena evolve in an organized rotating stall, as testified by the appearance of the corresponding frequency in the time domain. The mechanical power (fig. 27b) presents instantaneous negative values starting from 45%Q_{bep} but it is only for mass flow rates lower than 24.5%Q_{bep} that the machine is

characterized by a significant increase in oscillation amplitude with almost stable

negative values.

In order to better understand the reasons for this change in slope, the total head

H_d of the pump-turbine was decomposed on the basis of the contributions of the

different components of the pump-turbine (fig. 28):

$$H_d = H_{runner} + H_{GV} + H_{ducts} \qquad (7)$$

where H_{runner} and H_{GV} are the total pressure differences between inlet and outlet of the

runner and guide vanes respectively, and H_{ducts} is the sum of the total pressure

differences between inlet and outlet of the return channel, of the inlet duct and of the

draft tube.

As it can be seen in fig. 28, H_{runner} continuously decreases during the load

rejection simulation. The rotating stall, developing as demonstrated by the time-

frequency analysis from mass flow rates lower than 24.5% Q_{bep}, seems only to affect the

runner performance in terms of significant increase of the head oscillations causing, for

the lowest flow rates, an alternating behavior of the runner: from generating to reverse

pumping mode and vice-versa.

Since H_{ducts} is almost constant during the load rejection simulation, the most

important contribution to the increase in H_d is hence given by the guide vanes. H_{GV},

almost constant in the first part of the simulation, started to significantly increase from

a mass flow rate of about 24.5% Q_{bep}, that is from the development of the organized

rotating stall.

20

The fluid-dynamical reasons of this increase seem to be related to the behavior of the runner blades affected by the development of the rotating stall. It has been demonstrated that, for mass flow rates smaller than 24.5Q_{bep}, at each instant of the simulation, one or more runner blades behave as pump blades (fig. 15) because of the blockage of the channel on their pressure side. This determines a back flow in the channel on their suction sides (see for example fig. 16 – blade 4), interesting also some guide vanes channels. The mass flow rate flowing back in these guide vanes channels receives an increasing amount of energy by the runner due to the "pump blades" (i.e. pumping action of the blade-to-blade blocked passages), resulting in an increasing H_{GV}. In confirmation to this, in fig. 28 it is interesting to notice a certain opposite correspondence of humps and valleys between the increasing trend of H_{GV} and the decreasing one of H_{runner}.

So, even though the guide vanes provide the main contribution to the change in slope of the head-discharge curve, the fluid-dynamical reasons of this change should be ascribed to the development of the rotating stall in the runner, further confirming the results of the time-frequency analysis.

The negative slope of the total head curve (fig. 27a) determines an S-shaped characteristic in a dimensionless speed-discharge curve, whose speed and discharge factor are defined according to the IEC 60193 standard [23]:

$$n_{ED} = \frac{nD_2}{\sqrt{E}} \qquad (8)$$

$$Q_{ED} = \frac{Q}{D_2^2 \sqrt{E}} \qquad (9)$$

where D_2 is the outer runner diameter, n is the runner rotation velocity and E is the specific energy [J/kg].

Fig. 29 reports the dimensionless factors (eqs. 8 and 9) calculated in some operating points of the stable area (time-averaged values) and during load rejection (continuous line).

Interestingly, the development of unsteady phenomena inside the pump-turbine is not a sufficient condition for the S-shape feature of the discharge-speed curve. It is only their evolution in an organized rotating stall, characterized by a well-defined frequency that determines the change in slope of the n_{ED}-Q_{ED} curve with the appearance of the S-shape and, therefore, the resulting unstable behaviour of the pump-turbine. This also explains the reasons for the positive results in terms of stability obtained by particular procedures carried out during the synchronization, such as the misalignment of few guide vanes [23]. The resulting destruction of the flow symmetry prevents the development of the rotating stall, thereby avoiding the negative influence of the S-shape. However, this solution also presents significant drawbacks, since it increases hydraulic system oscillations and pressure pulsations in the draft tube as well as unbalanced radial forces on the runner [10].

6. CONCLUSIONS

The S-shaped characteristic in pump-turbines is associated with the development of an unstable behavior with fluctuations of speed, torque, head and flow rate that negatively affect the start-up and synchronization of the pump-turbine with the grid as well as load rejection scenario.

This paper presents an in-depth study of the onset and development of the unsteady phenomena that cause the unstable behavior of a pump-turbine during a load rejection scenario with servomotor failure.

To validate the numerical model, transient numerical analyses were carried out on a pump-turbine in stable operating conditions and the numerical performance results were compared with the experimental ones, obtaining a satisfactory agreement. Subsequently, starting from a stable operating condition, a numerical analysis running through the speed-discharge characteristics up to the pump-turbine brake zone was performed. The flow field evolution was analysed for about 20 impeller revolutions with a flow rate slowly decreasing at each time step in order to simulate the real behavior of the pump-turbine during a load rejection scenario.

Running through the unstable operating zone, the analysis made it possible to identify the onset and the development of stalled cells partially or totally blocking some runner and distributor channels. These cells moved from one channel to the next with increasing intensity. Their onset, enlargement and disappearance was shown to cause fluctuations over time, not only of the flow rate passing through the channels both in the runner and in the guide vanes, but also of the pressure distribution and hence of the torque exerted on the blades, with possible negative effects on the mechanical fatigue of the blades.

These fluctuations increased in amplitude together with the intensity of the unsteady phenomena and, for low flow rates, became so intense as to cause continuous changes in blade operating mode (from turbine to reverse pump and vice-versa).

These unsteady phenomena were characterized by a well-defined frequency (65.1% of the runner rotation frequency; $St_{RS,st}=0.093$ in stationary frame) starting to appear in the spectrum for flow rates lower than 24.5%. It was demonstrated that only at this operating condition, corresponding to a complete development of an organized rotating stall in the runner, does the slope of the head curve change, bringing about the S-shape in the discharge-speed dimensionless curve. Even though the guide vanes results to provide the main contribution to the increase in the pump-turbine head in the turbine brake operating area, the fluid-dynamical reasons of it were ascribed to the blockage action of the rotating stall development in the runner, which causes some runner blades to behave as pump blades.

Summing up, the onset of unsteady phenomena in the pump-turbine is not a sufficient condition for giving rise to the S-shape feature in the dimensionless characteristic curve. Only when they evolved in a fully-developed rotating stall characterized by a well-defined frequency, did the head start to increase causing the S-shape, suggesting that proper design criteria aimed at moving this critical operating point at lower flow rates could further limit or eliminate the unstable behavior of the pump-turbine in turbine mode. It must be pointed out that these results refer to the particular pump-turbine geometry (single stage of a two-stage regulated pump-turbine) analysed in this study. However, because of the good agreement with the results of other studies published on the topic, they can be considered reasonably transferable to the more common reversible single stage pump-turbines.

AKNOWLEDGMENTS

NOMENCLATURE

B	width, mm
C_m	meridional absolute velocity component, m/s
C	blade mean line, m
D	diameter, m
E	specific energy, J/kg
F	frequency, Hz
$G^{xx}(f)$	auto-spectrum of the signal x
$G^{xy}(f)$	cross-spectrum of the signals x and y
g	gravitational acceleration, m/s^2
H	head, m
K	reduction rate, kg/s^2
P	mechanical power, kW
p	pressure, Pa
Q	flow rate, m^3/s
$Q_{ED} = \dfrac{Q}{D_i^2 \sqrt{E}}$	discharge factor, -
Q_m	mass flow rate, kg/s
$q_{i,Q}$	flow rate of the channel i, m^3/s

$St=\pi D_2 f/n_b U_2$ Strouhal number based on the blade passage frequency

s wavelet scale

n rotation velocity, rpm

n_b number of blades, -

$n_{ED}=\dfrac{nD_2}{\sqrt{E}}$ speed factor, -

$n_s=nQ^{0.5}/h^{0.75}$ specific speed, -

$n*$ time index of a signal, Nm

T torque, Nm

t time, s

U peripheral velocity, m/s

u,v,w absolute velocity components, m/s

$X(f)$ Fourier transform of the signal x

$Y(f)$ Fourier transform of the signal y

W_H Hanning windowing weighting constant

$W(s,n*)$ continuous wavelet transform

Greek Symbols

α absolute flow angle, °

β relative flow angle, °

ε fluctuation of the instantaneous flow rate passing through a blade-to-

	blade channel,-
η	efficiency, -
λ	stagger angle, °
ρ	water density, kg/m^3
$\phi=C_{m2}/U_2$	flow coefficient, -
ω	angular rotation velocity, rad/s
$\omega_s=\omega Q^{0.5}/(gh)^{0.75}$	dimensionless specific speed, -

Acronyms

BC	boundary condition
GVO	guide vane opening
PS	pressure side
RMS	root mean square
RPT	reversible pump-turbine
SS	suction side

Subscripts

1	runner outlet
2	runner inlet
3	adjustable guide vanes outlet
4	adjustable guide vanes inlet

bep	best efficiency point
BPF	blade passage frequency
ducts	inlet and outlet duct
GV	adjustable guide vane
RS	rotating stall
r	runner
rot	rotating reference frame
rr	runner rotation frequency
st	stationary reference frame

REFERENCES

[1] Ardizzon, G., Cavazzini, G. and Pavesi, G., 2014, "A new generation of small hydro and pumped-hydro power plants: advances and future challenges," Ren Sustain Energy Rev, **31**, pp. 746-76. DOI: 10.1016/j.rser.2013.12.043

[2] Fisher, R., Koutnik, J., Meier, L., Loose, V., Engels, K., and Beyer, T., 2012, "A Comparison of Advanced Pumped Storage Equipment Drivers in the US and Europe," *HydroVision 2012*, Louisville, KY, 18 July 2012. DOI: 10.13140/2.1.1082.4967

[3] Zhou, J. X., Karney, B.W., and Xu, J.C., 2011, "Analytical study on possible self-excited oscillation in S-shaped regions of pump turbines," P I Mech Eng A – J POW, **225**(8), pp. 1132-1142. DOI: 10.1177/0957650911419442

[4] Gentner, C., Sallaberger, M., Widmer, C., Braun, O., and Staubli, T., 2012, "Analysis of unstable operation of pump turbines and how to avoid it," *HYDRO 2012 Innovative Approaches to Global Challenges*, Bilbao, Spain, 29-31 October 2012.

[5] Pejovic, S., Zhang, Q.F., Karney, B., and Gajic, A., 2011, "Analysis of pump-turbine S instability and reverse waterhammer incidents in hydropower systems," *4th Int Meeting on Cavitation and Dynamic problems in Hydraulic Machinery Systems*, Belgrade, Serbia, October 2011.

[6] Olimstad, G., Nielsen, T., and Børresen, B., 2012, "Dependency on runner geometry for reversible pump turbine characteristic in turbine mode of operation," ASME J Fluids Eng, **134**, pp. 121102-1/9. DOI: 10.1115/1.4007897

[7] Olimstad, G., Nielsen, T., and Børresen, B., 2012, "Stability limits of reversible pump turbines in turbine mode of operation and measurements of unstable characteristic," ASME J Fluids Eng, **134**, pp. 111202-01/08. DOI:10.1115/1.4007589

[8] Seidel, U., Koutnik, J., and Martin, G., 2012, "S-curve characteristic of pump-turbines," *HYDRO 2012 Innovative Approaches to Global Challenges*, Bilbao, Spain, 29-31 October 2012.

[9] Wang, L.Q., Yin, J.L., Jiao, L., Wu, D., and Qin, D., 2011, "Numerical investigation on the "S" characteristic of a reduced pump turbine model," Sci China Ser E, **54**(5), pp. 1259-1266. DOI: 10.1007/s11431-011-4295-2

[10] Sun, H., Xiao, R., Liu, W., and Wang, F., 2013, "Analysis of the S characteristic and pressure pulsation in a pump turbine with misaligned guide vanes," ASME J Fluids Eng, **135**(5), pp. 051101-1/6. DOI: 10.1115/1.4023647

[11] Brennen, C.E. 1994, *Hydrodynamics of pumps*, Oxford University Press, Oxford, UK. ISBN 0-19-856442-2

[12] Hasmatuchi, V., Farhat, M., Roth, S., Botero, F., and Avellan, F., 2011, "Experimental evidence of rotating stall in a pump turbine at off design conditions in generating mode," ASME J Fluids Eng, **133**(5), pp. 051104-1/8. DOI: 10.1115/1.4004088

[13] Hasmatuchi, V., Farhat, M., Roth, S., Botero, F., and Avellan, F., 2011, "Hydrodynamics of a pump turbine at off design conditions in generating mode: experimental investigation," *SHF Conference on Cavitation and Hydraulic Machines*, Lausanne, Switzerland, 26-27 May 2011.

[14] Widmer, C., Staubli, T., and Ledergerber, N., "Unstable Characteristics and Rotating Stall in Turbine Brake Operation of Pump-Turbines," ASME J Fluids Eng, **133**, pp. 041101-1/9. DOI: 10.1115/1.4003874

[15] Botero, F., Hasmatuchi, V., Roth, S., and Farhat, M., 2014, "Non-intrusive detection of rotating stall in pump-turbines," Mech Syst Signal Process, in press. DOI: 10.1016/j.ymssp.2014.03.007

[16] Houdeline, J.-B., Liu, J., Lavigne, S., Laurant, Y., and Balarac, L., 2011, "Start-up improvement in turbine mode for high head PSP machine," IOP Conference Series: Earth and Environmental Science, **15**(4), pp. 1-10. DOI:10.1088/1755-1315/15/4/042022

[17] Yin, J., Wang, D., Wei, X., and Wang, L., 2013, "Hydraulic Improvement to Eliminate S-Shaped Curve in Pump Turbine," ASME Journal of Fluids Engineering, **135**, pp. 0711105-1/6. DOI: 10.1115/1.4023851

[18] Yang J., Pavesi G., Yuan S., Cavazzini G. and Ardizzon G., 2015, "Experimental Characterization of a Pump–Turbine in Pump Mode at Hump Instability Region", ASME J Fluids Eng, **137**(5), pp. 051109-1/11. DOI: 10.1115/1.4029572

[19] Pavesi, G., Cavazzini, G., and Ardizzon, G., 2008, "Time-frequency characterization of the unsteady phenomena in a centrifugal pump," I J Heat Fluid Flow, **29**, pp. 1527-1540. DOI:10.1016/j.ijheatfluidflow.2008.06.008

[20] Krause, N., Zähringer, K., and Pap, E., 2005, "Time-Resolved Particle Image Velocimetry for the Investigation of Rotating Stall in a Radial Pump," Exp Fluids, **39**, pp. 192-201. DOI: 10.1007/s00348-005-0935-2

[21] Lucius, A., and Brennen, G., 2011, "Numerical Simulation and Evaluation of Velocity Fluctuations During Rotating Stall of a Centrifugal Pump," ASME J Fluids Eng, **133**(8), pp. 081102-1/8. DOI:10.1115/1.4004636

[22] Farge, M., 1992, "Wavelet transforms and their application to turbulence," Annu Rev Fluid Mech, **24**, pp. 395-457. DOI: 10.1146/annurev.fl.24.010192.002143

[23] Shao, W.Y., 2009, "Improving Stability by Misaligned Guide Vanes in Pumped Storage Plant," *Asia-Pacific Power and Energy Engineering Conference*, Wuhan, China, 28-31 March 2009, pp. 1–5.

Figure Captions List

Fig. 1   S-shaped characteristic curve of a pump-turbine in generating mode: discharge-speed curve at a constant guide vane opening
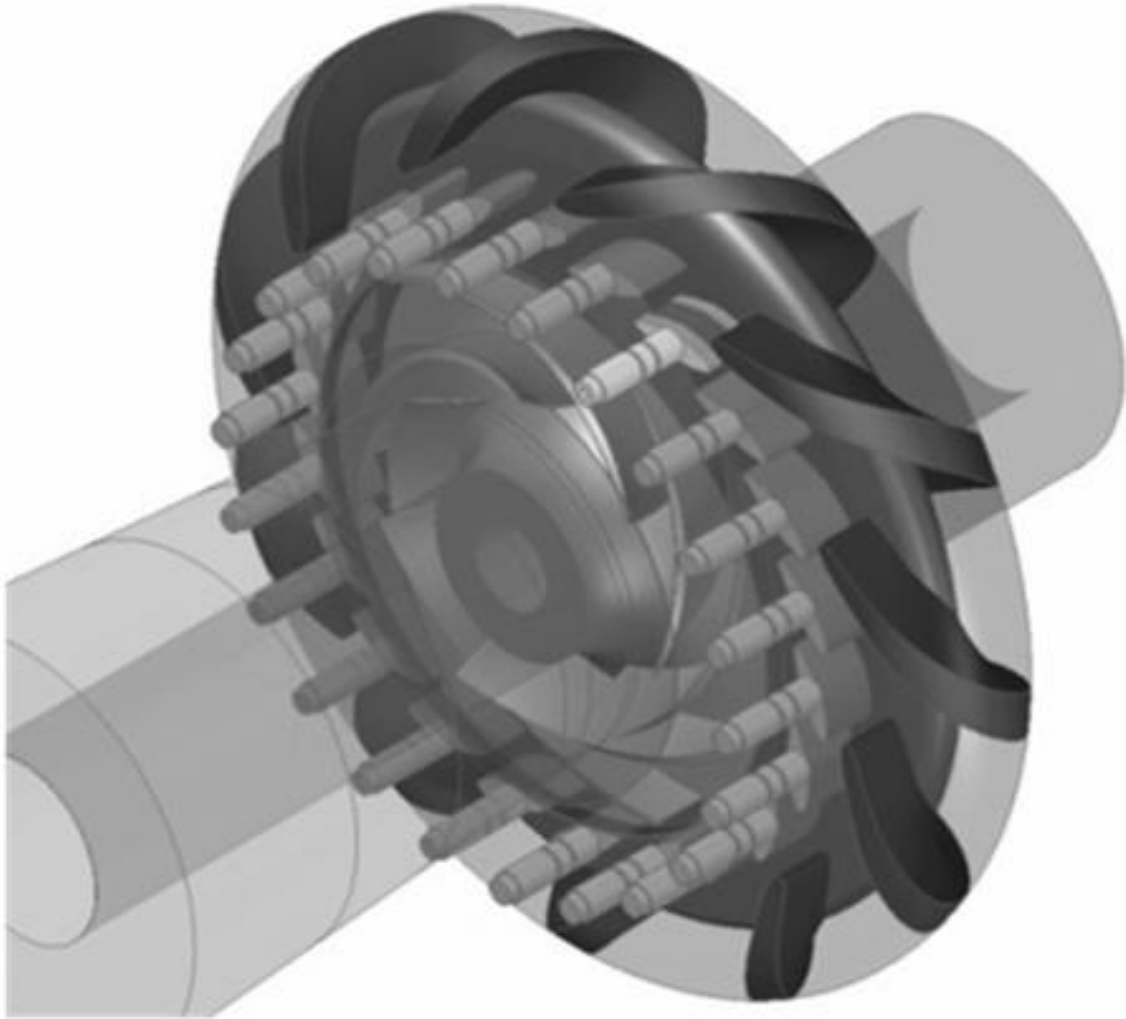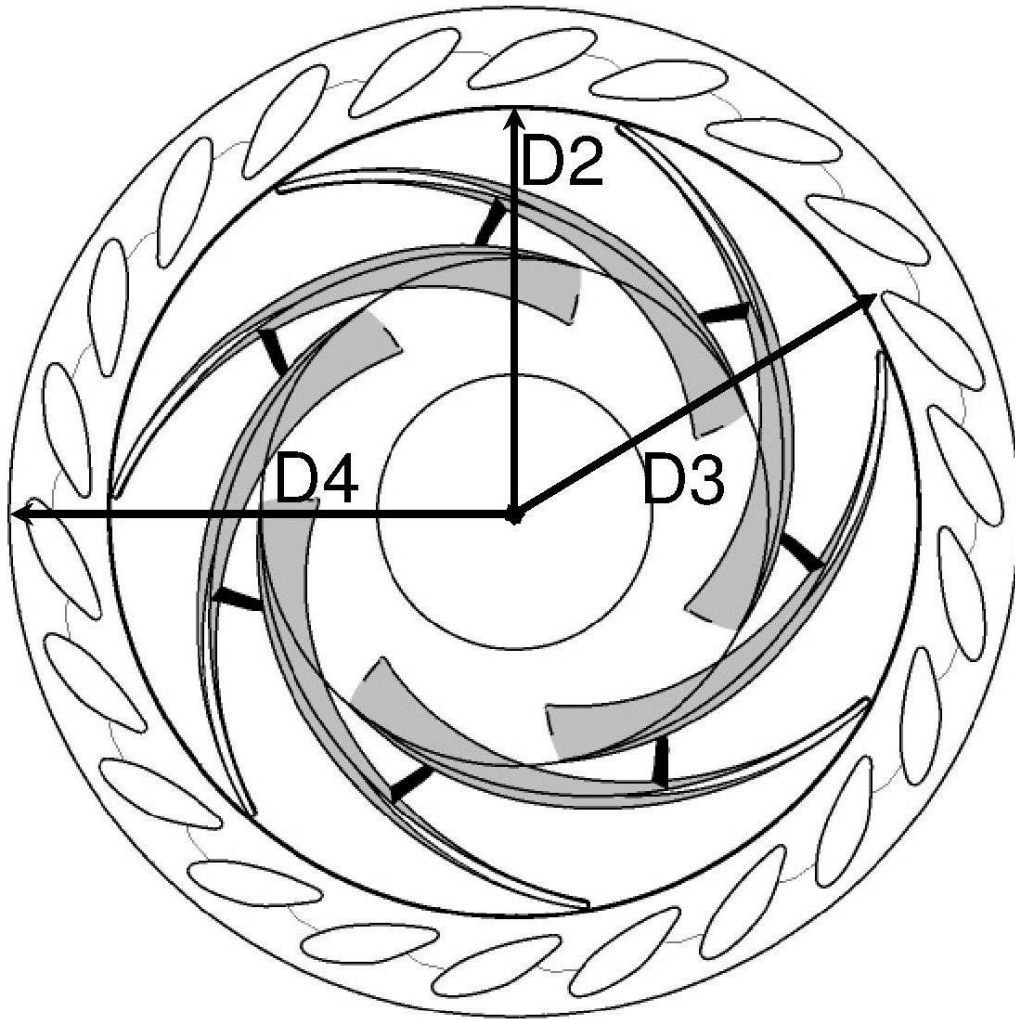
Fig. 2   Scheme of the tested configuration

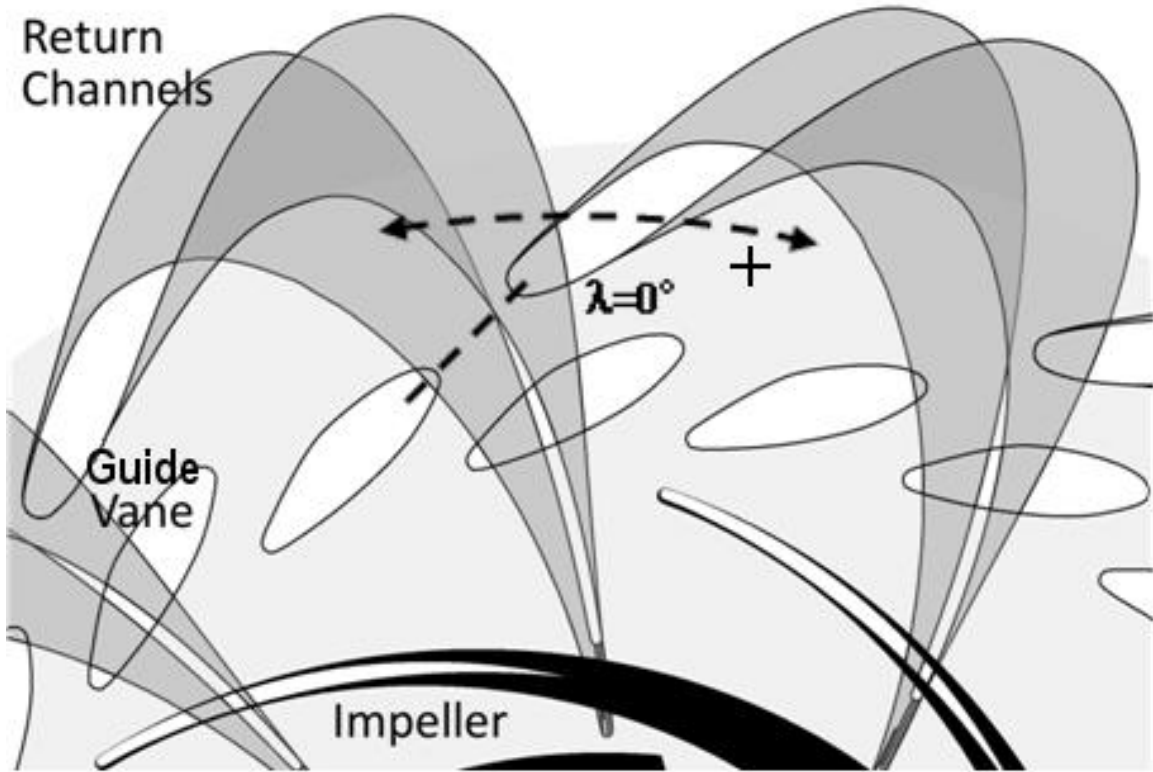Fig. 3   Sketch of the runner and distributor with references of the main diameters

Fig. 4   Guide vanes reference position ($\lambda=0°$)
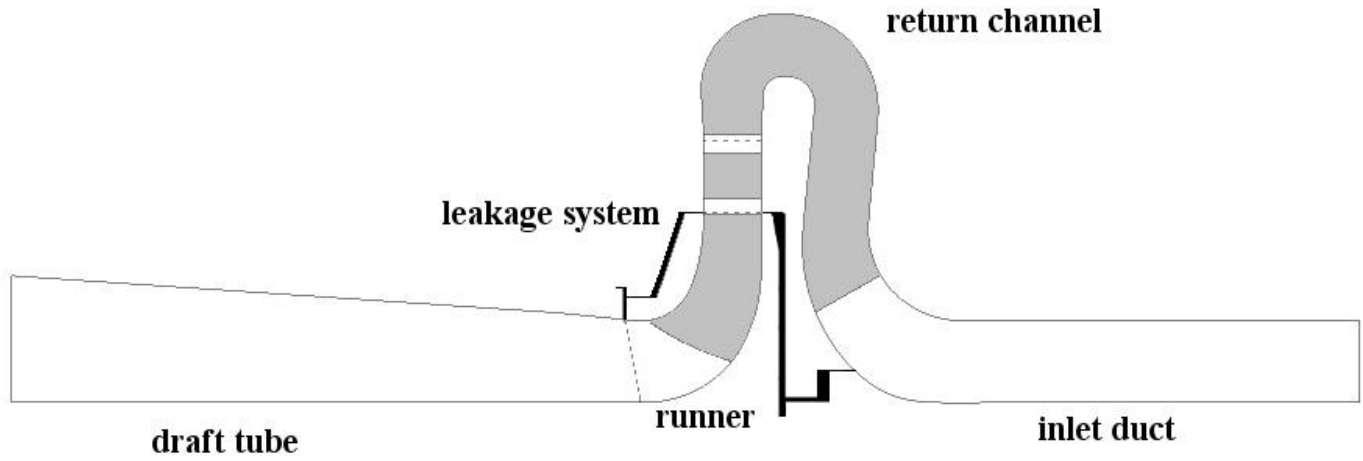
Fig. 5   Meridional view of the numerical model. Regions filled in grey refer to the blades; region filled in black refers to the leakage system.
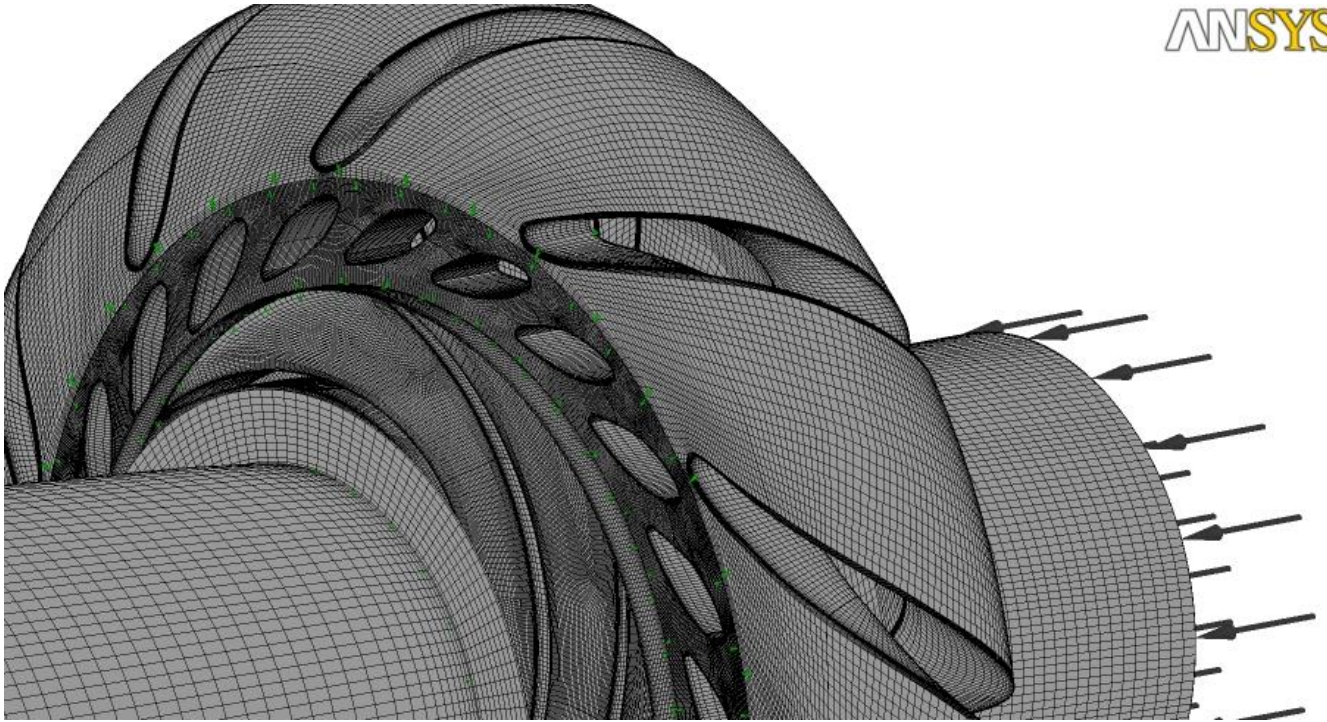
Fig. 6   Detail of the coarse mesh of the numerical model: inlet duct, return channel, guide vanes, runner, draft tube and part of the meshed leakage system.
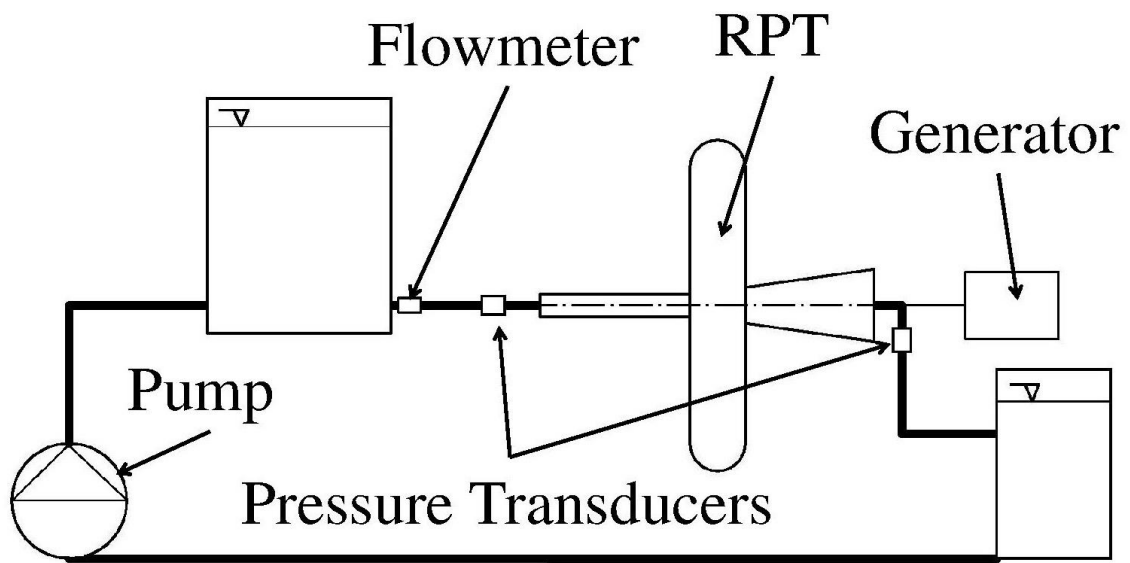
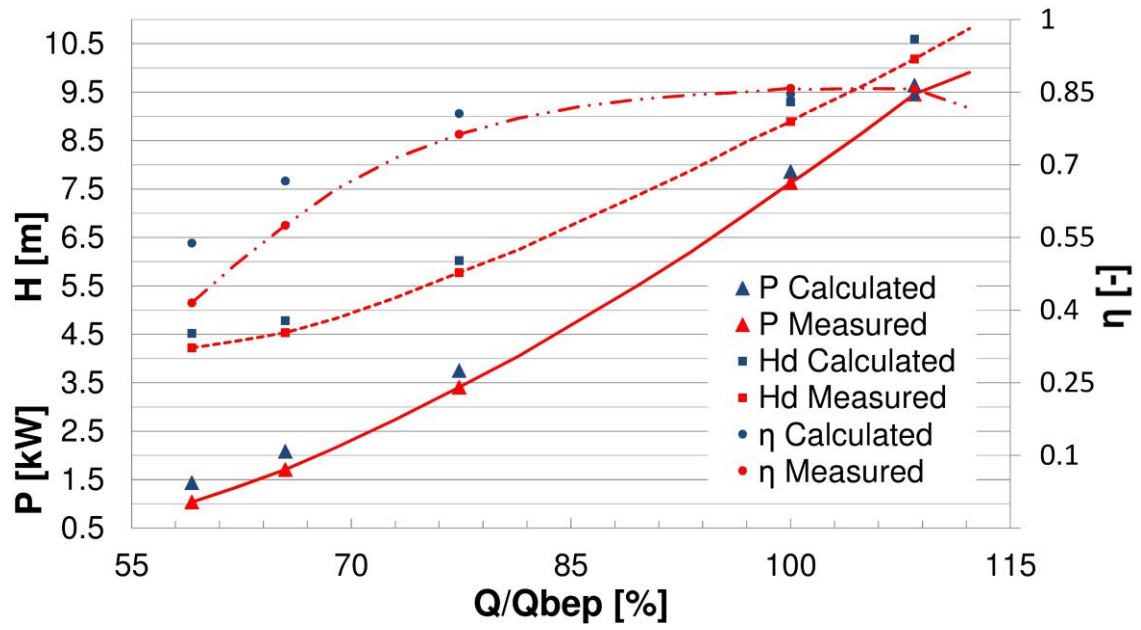Fig. 7   Scheme of the experimental set-up

Fig. 8   Comparison between numerical and experimental performance curves
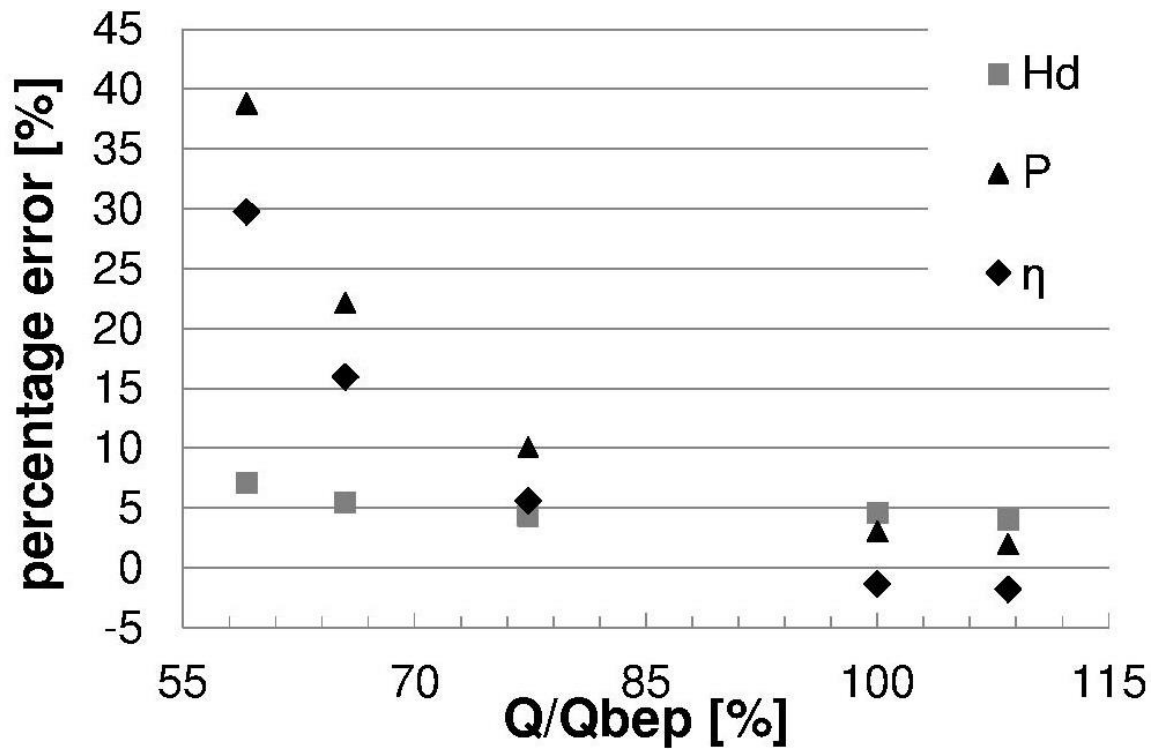
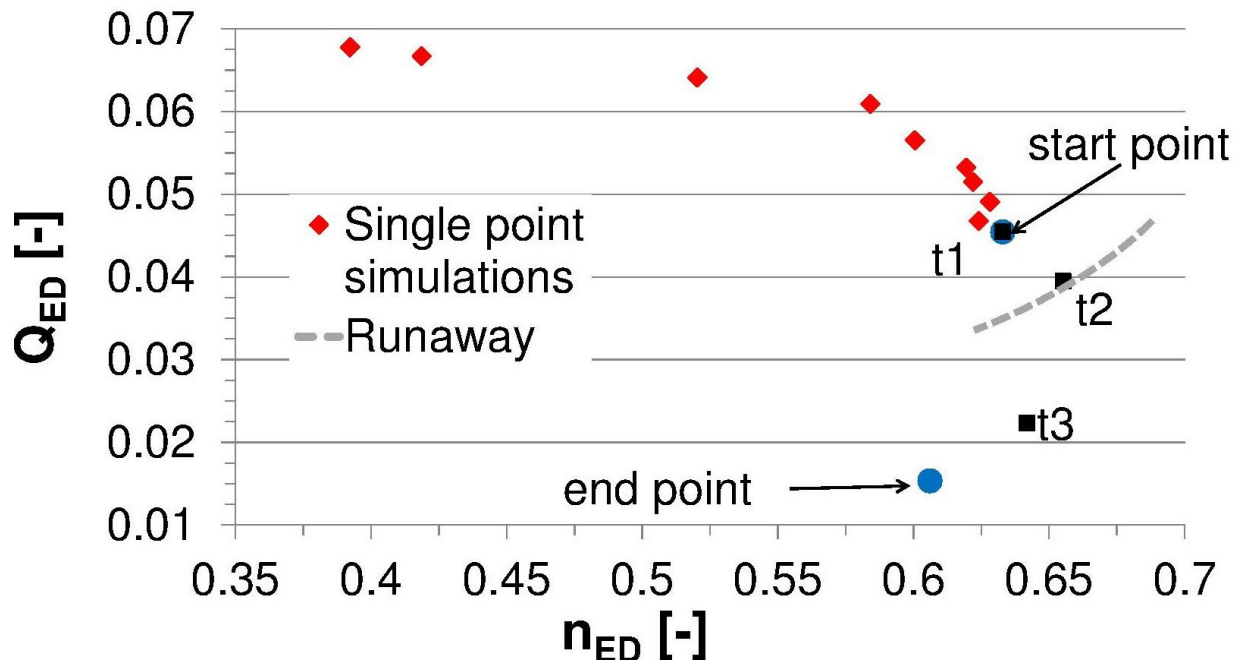Fig. 9   Percentage errors in performance between experimental and numerical results

Fig. 10   Starting and ending points of the numerical simulation of the turbine brake (at constant GVO and constant speed)
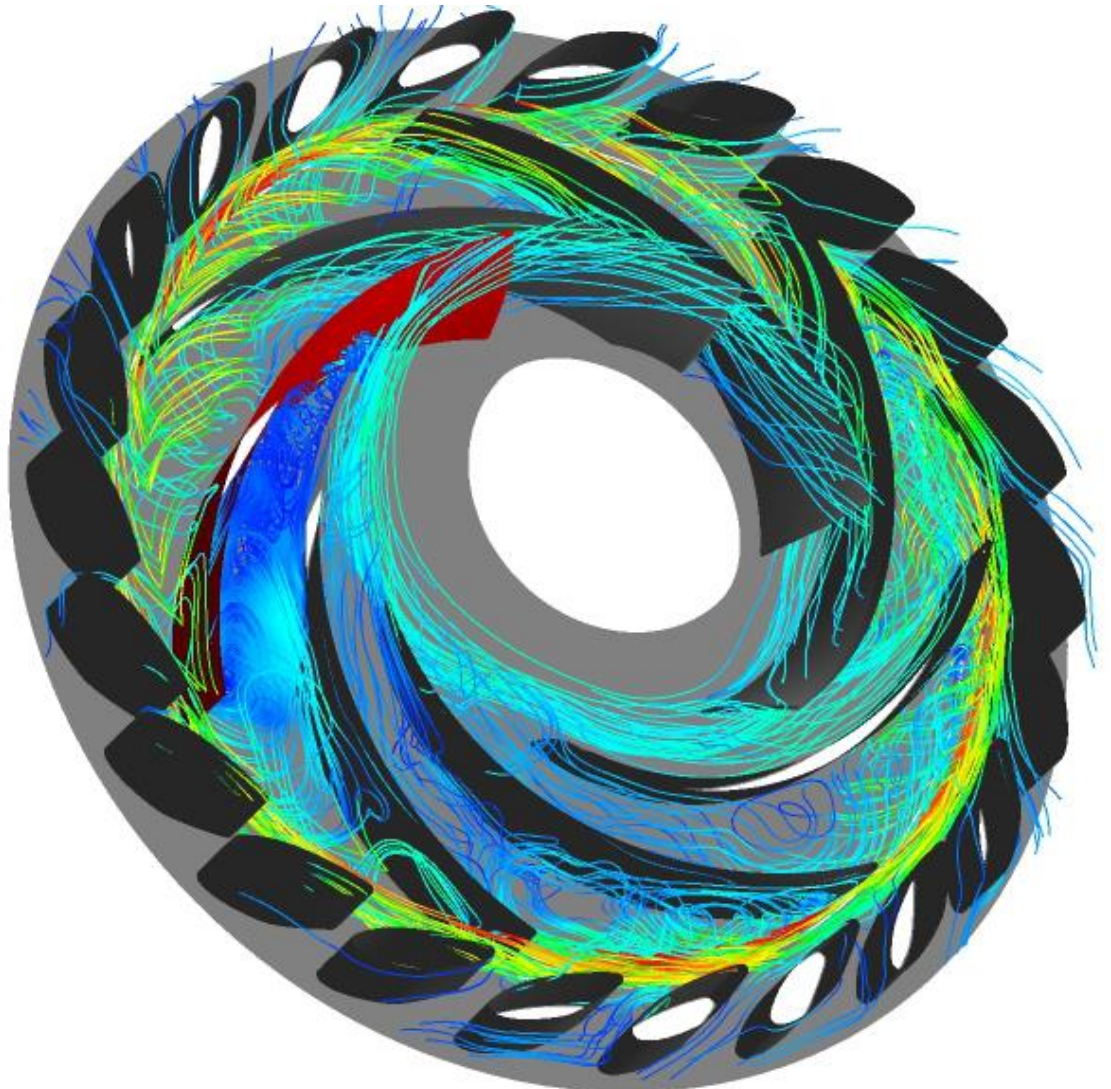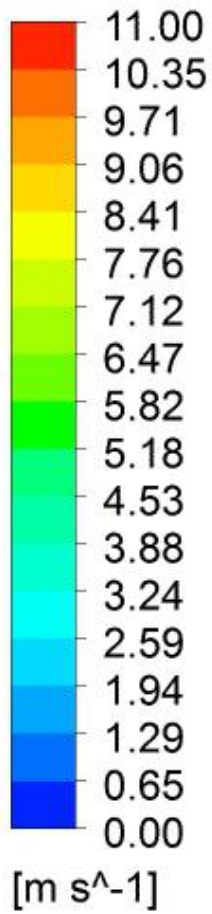
Fig. 11   Flow pattern in the unstable branch of the characteristic ($Q=21.8\%Q_{bep}$) inside the runner (relative streamlines) and inside the guide vanes
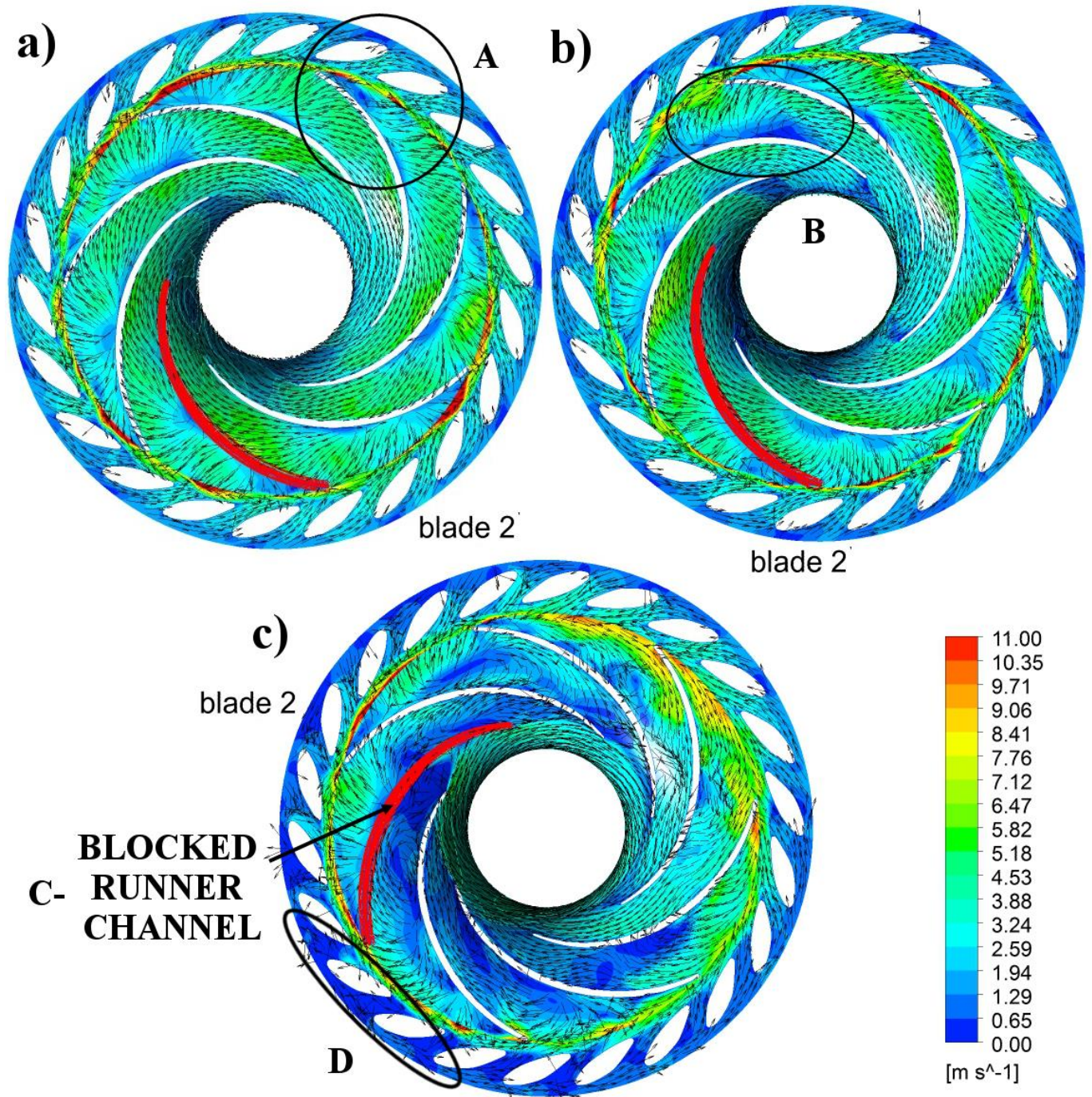
(absolute streamlines)

Fig. 12   Instantaneous velocity flow field inside runner and guide vanes at midspan at three different instants: a) t1 – Q= 45.1%Q_{bep}; b) t2 – Q=37.8%Q_{bep}; c) t3 – Q=21.8%Q_{bep}
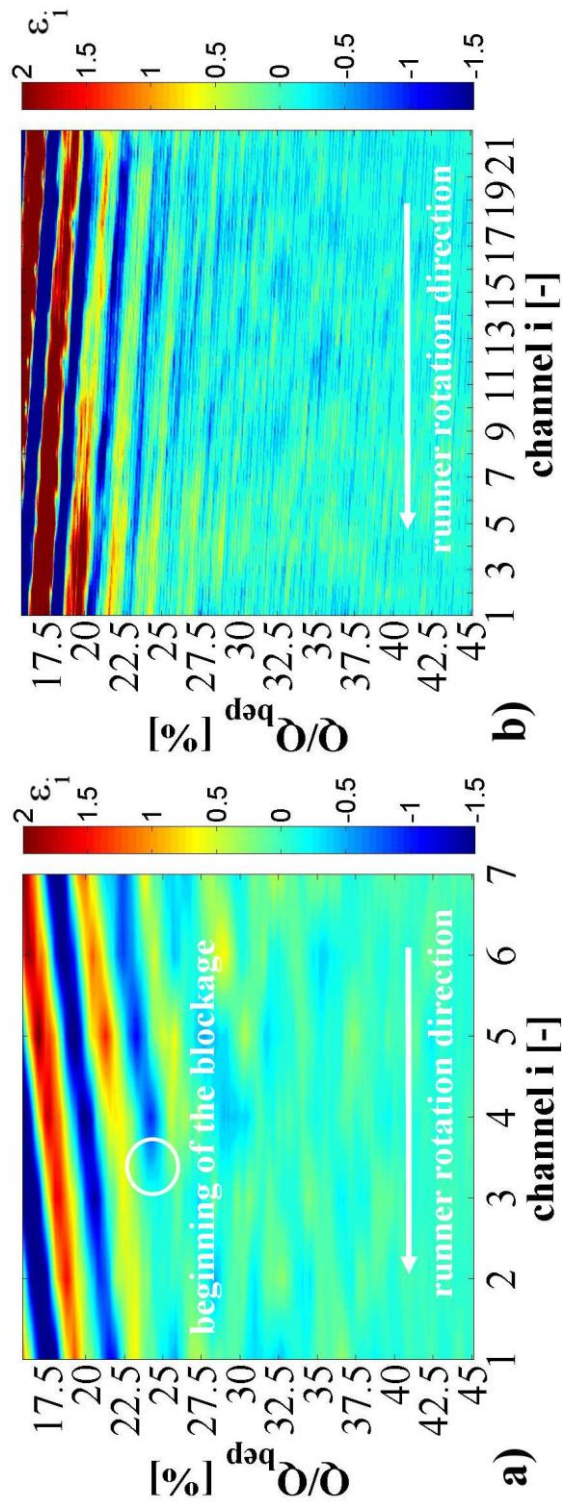
Fig. 13   Evolution of the instantaneous flow rate passing through each channel of the runner a) and of the guide vanes b) during the turbine brake. $\varepsilon_i = -1$ means blocked channel; $\varepsilon_i < -1$ means back flow in the channel

Fig. 14   Pressure profiles on a runner blade (blade 2) at mid-span at four different instants: a) Q= 45.1%Q_{bep}; b) Q=37.8%Q_{bep}; c) Q=21.8%Q_{bep}

Fig. 15   Evolution of the blade torque during the turbine brake: a) runner (blades 2,4 and 6); b) guide vanes (blades 1, 7, 13 and 19)

Fig. 16   Flow field inside runner and guide vanes for Q= 20.3%Q_{bep}: a) flow pattern by means of absolute (guide vanes) and relative (runner) streamlines; b) Instantaneous velocity flow field at mid-span

Fig. 17   Scheme of the positions of the acquired numerical signals

Fig. 18   Power-spectra of the mass flow rates through runner channels (a) and of the torques acting on the runner blades (b)

Fig. 19   Power-spectra of the mass flow rates through the distributor channels (a) and of the torques (b) acting on 7 guide vanes blades

Fig. 20   Power-spectra of the static pressure signals acquired at the guide vanes inlet (a) and outlet (b)

Fig. 21   Cross-spectra of the mass flow rates a) and torque signals b) between

different runner blades

Fig. 22   Cross-spectra of the mass flow rates a) and torque signals b) between

different guide vanes

Fig. 23   Cross-spectra of the static pressure at a) guide vanes outlet and b) guide

vanes inlet

Fig. 24   Wavelets of a) the mass flow rate in runner channel 2 and b) of the

torque acting on runner blade 2

Fig. 25   Wavelets of a) the mass flow rate in guide vanes channel 1 and b) of the

torque acting on guide vanes blade 1

Fig. 26   Wavelets of static pressure data series at a) $p^{3,1}$ and b) $p^{4,1}$

Fig. 27   Performance curve of the pump-turbine: a) head; b) mechanical power

Fig. 28   Contributions in head of the runner and guide vanes

Fig. 29   Numerical dimensionless discharge-speed curve

Table Caption List

Table 1   Pump-turbine data

Table 2   Mesh data
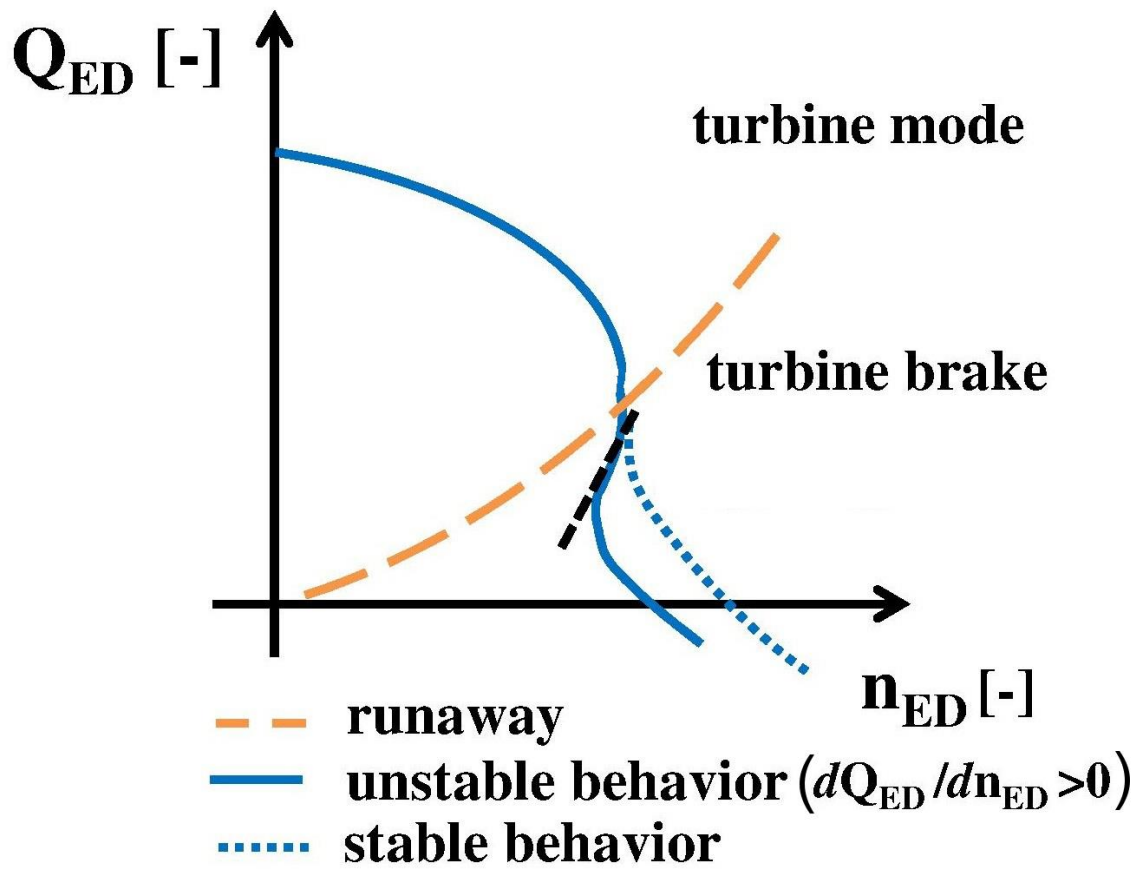
Fig. 1   S-Shaped characteristic curve of a pump-turbine in generating mode: discharge-speed curve at a constant guide vane opening

Fig. 2   Scheme of the tested configuration

Fig. 3 Sketch of the runner and distributor with references of the main diameters

Fig. 4   Guide vanes reference position (λ=0°)

Fig. 5   Meridional view of the numerical model. Regions filled in grey refer to the blades. Regions filled in black refer to the leakage system.

Fig. 6 Detail of the coarse mesh of the numerical model: inlet duct, return channel, guide vanes, runner, draft tube and part of the meshed leakage system.

Fig. 7 Scheme of the experimental set-up

Fig. 8   Comparison between numerical and experimental performance curves

Fig. 9 Percentage errors in performance between experimental and numerical results

Fig. 10 Starting and ending points of the numerical simulation of the turbine brake (at constant GVO and constant speed)

Fig. 11 Flow pattern in the unstable branch of the characteristic (Q=21.8%Q_{bep}) inside the runner (relative streamlines) and inside the guide vanes (absolute streamlines)

Fig. 12 Instantaneous velocity flow field inside runner and guide vanes at three different instants: a) t_1 – Q= 45.1%Q_{bep}; b) t_2 – Q=37.8%Q_{bep}; c) t_3 – Q=21.8%Q_{bep}

Fig. 13 Evolution of the instantaneous fluctuations ε of flow rate passing through each channel of the runner a) and of the guide vanes b) during the turbine brake. ε_i=-1 means blocked channel; ε_i<-1 means back flow in the channel

Fig. 14   Pressure profiles on a runner blade (blade 2) at mid-span at four

different instants: a) Q= 45.1%Q_{bep}; b) Q=37.8%Q_{bep}; c) Q=21.8%Q_{bep}

Fig. 15   Evolution of the blade torque during the turbine brake: a) runner (blades

2,4 and 6); b) guide vanes (blades 1, 7, 13 and 19)

Fig. 16   Flow field inside runner and guide vanes for Q= 20.3%Q_{bep}: a) flow pattern by means of absolute (guide vanes) and relative (runner) streamlines; b) Instantaneous velocity flow field at mid-span

Fig. 17   Scheme of the positions of the acquired numerical signals

a)

b)

Fig. 18   Power-spectra of the mass flow rates through runner channels (a) and of

the torques acting on the runner blades (b)

Fig. 19   Power-spectra of the mass flow rates through the distributor channels

(a) and of the torques (b) acting on 7 guide vanes blades

Fig. 20   Power-spectra of the static pressure signals acquired at the guide vanes

outlet (a) and inlet (b)

Fig. 21   Cross-spectra of the mass flow rates a) and torque signals b) between

different runner blades
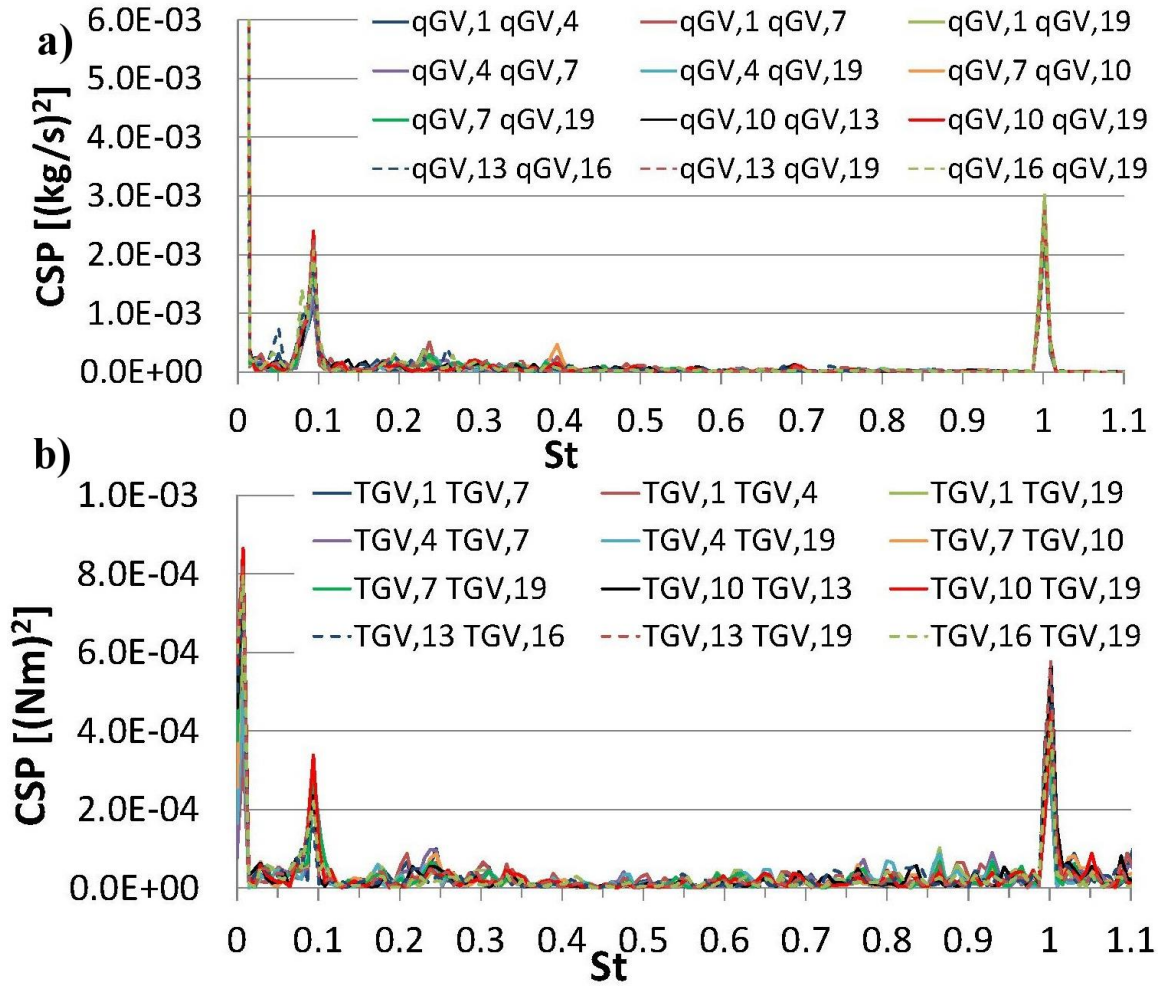
Fig. 22   Cross-spectra of the mass flow rates a) and torque signals b) between

different guide vanes
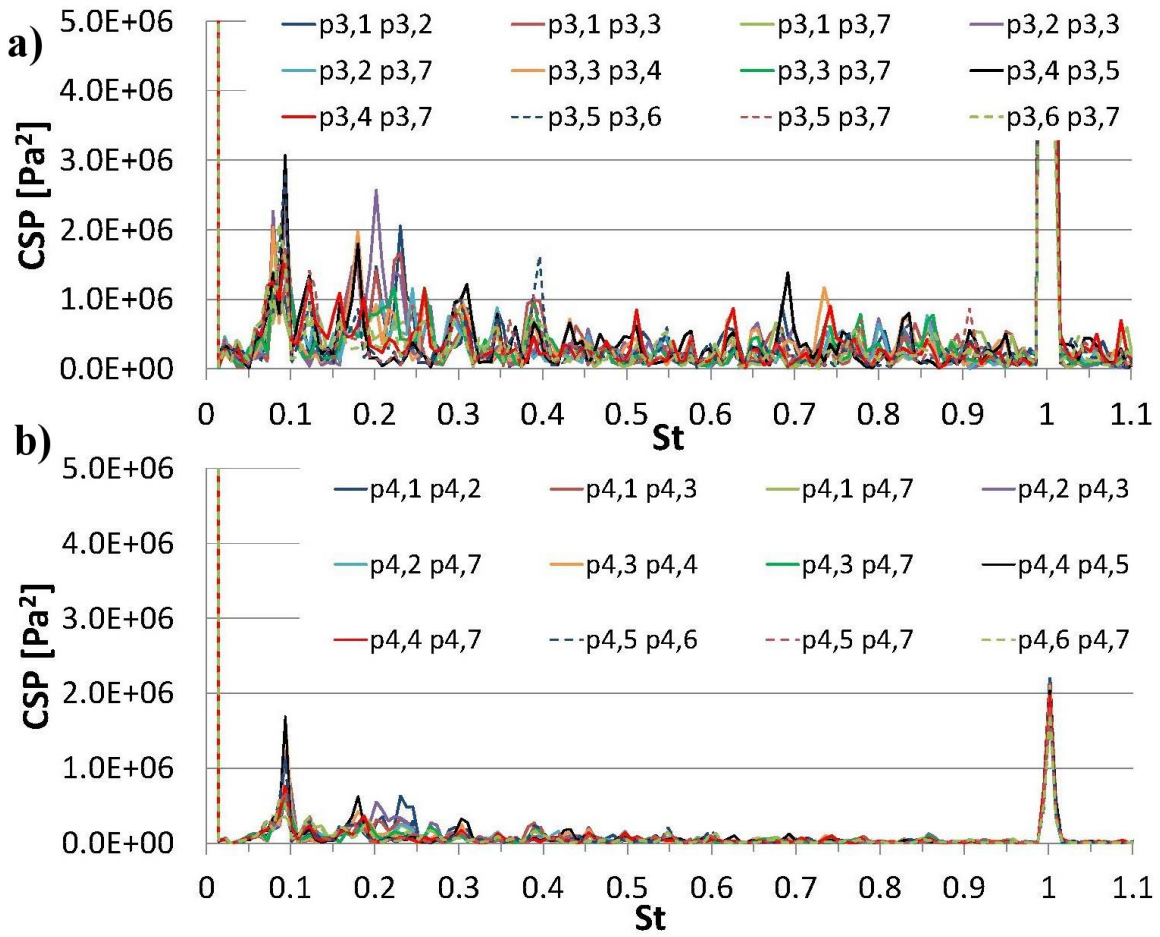
Fig. 23   Cross-spectra of the static pressure at a) guide vanes outlet and b) guide

vanes inlet
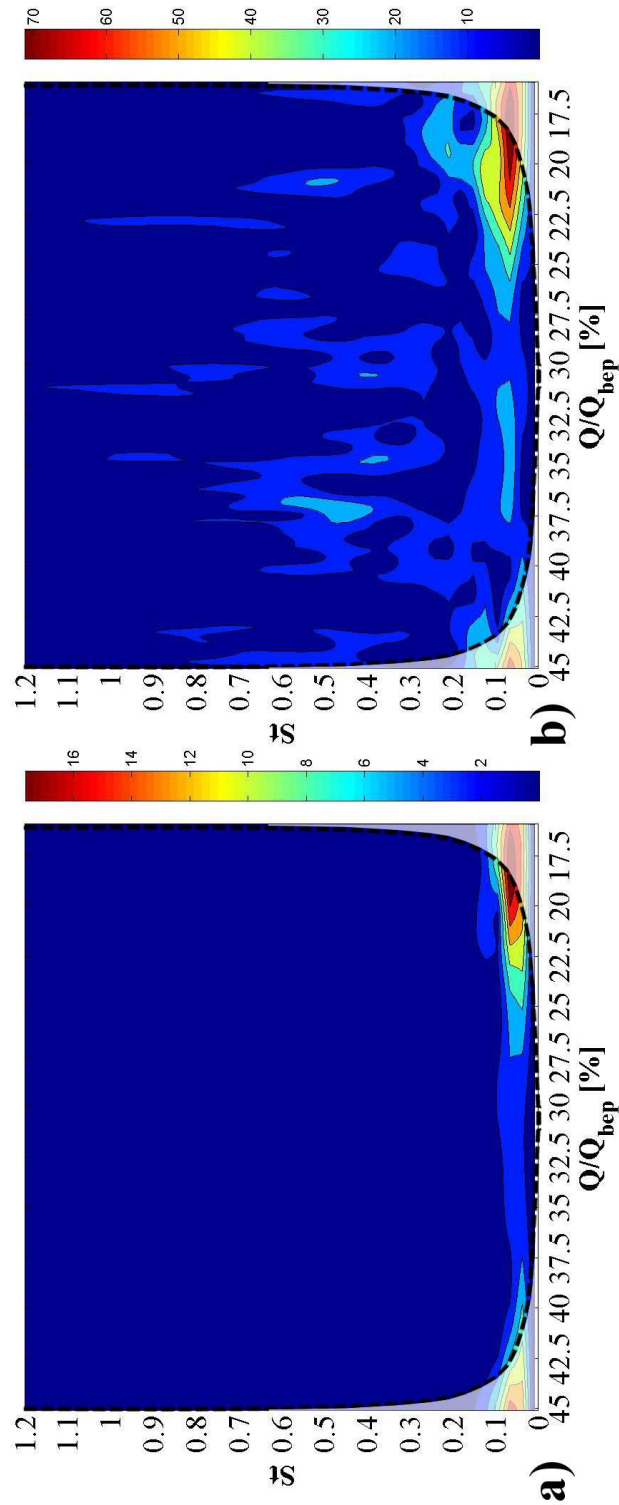
Fig. 24 Wavelets of a) the mass flow rate in runner channel 2 and b) of the torque acting on runner blade 2. The broken line indicate the "cone of influence", where edge effects become important.
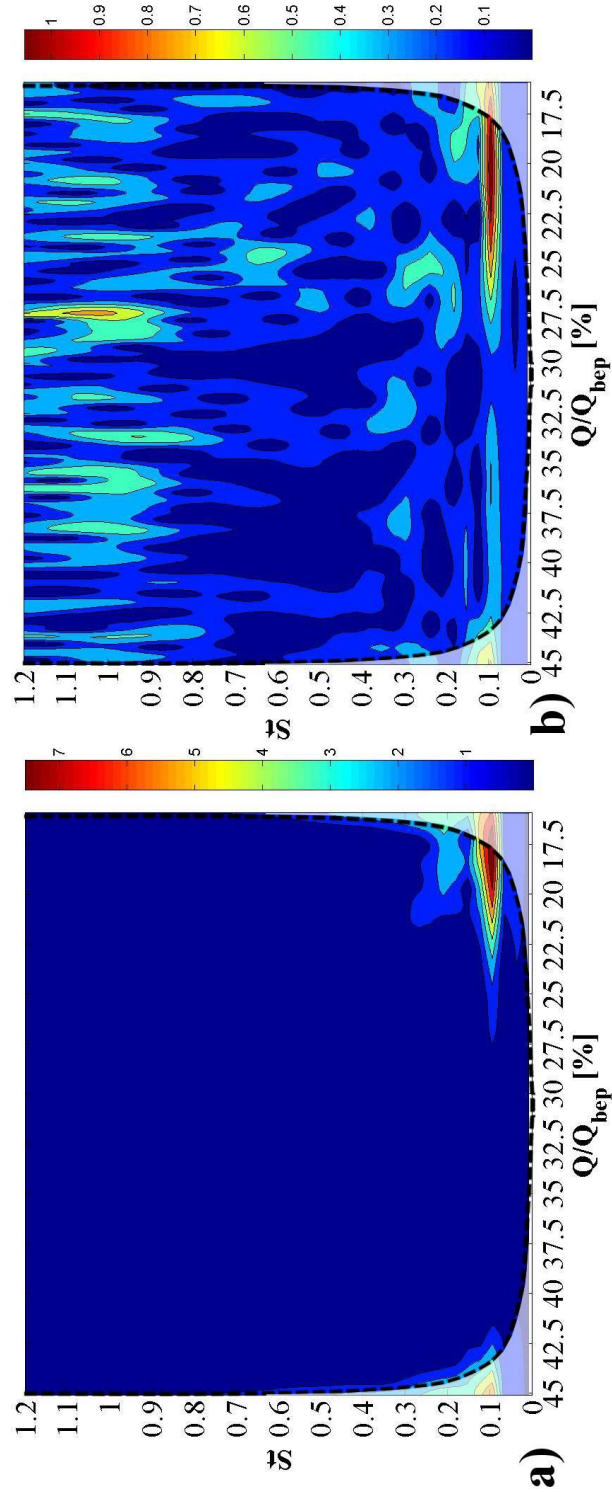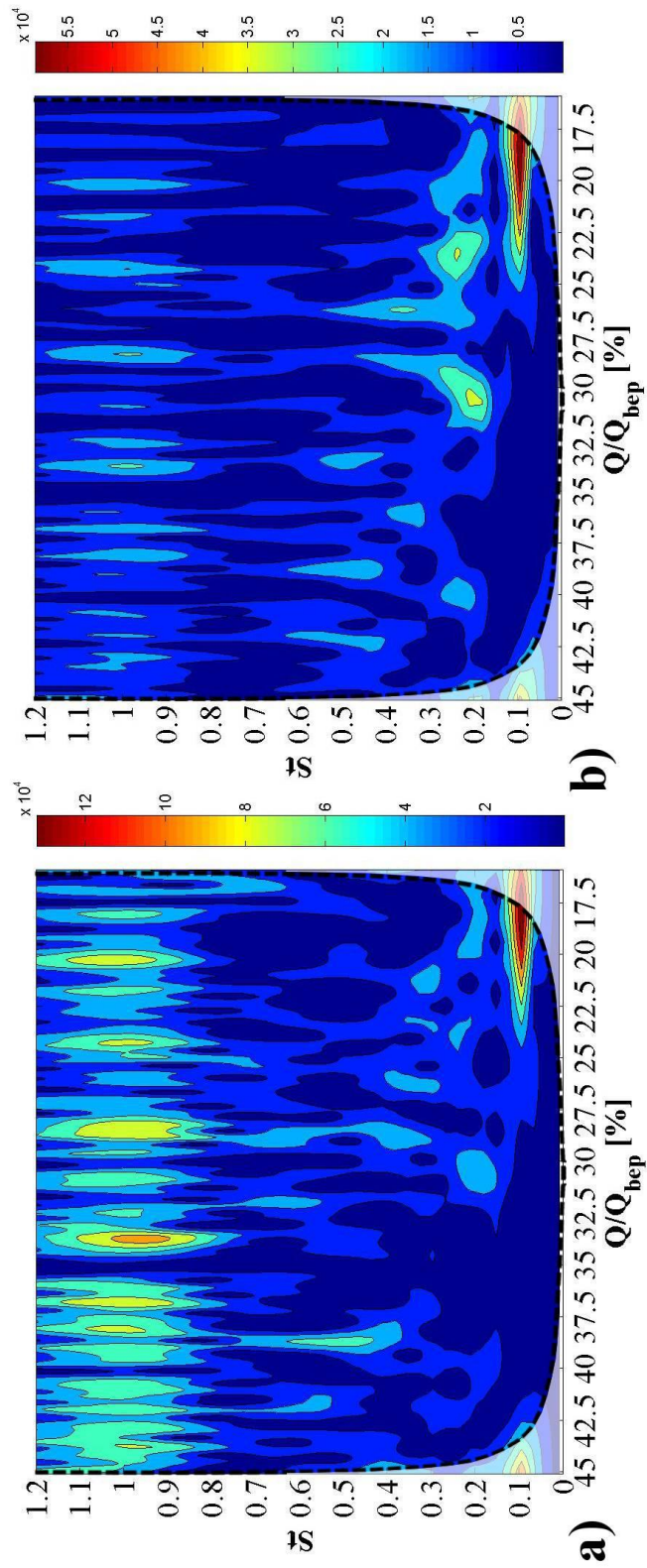
Fig. 25 Wavelets of a) the mass flow rate in guide vanes channel 1 and b) of the torque acting on guide vanes blade 1. The broken line indicate the "cone of influence", where edge effects become important.

Fig. 26 Wavelets of static pressure data series at a) $p^{3,1}$ and b) $p^{4,1}$. The broken line indicate the "cone of influence", where edge effects become important.
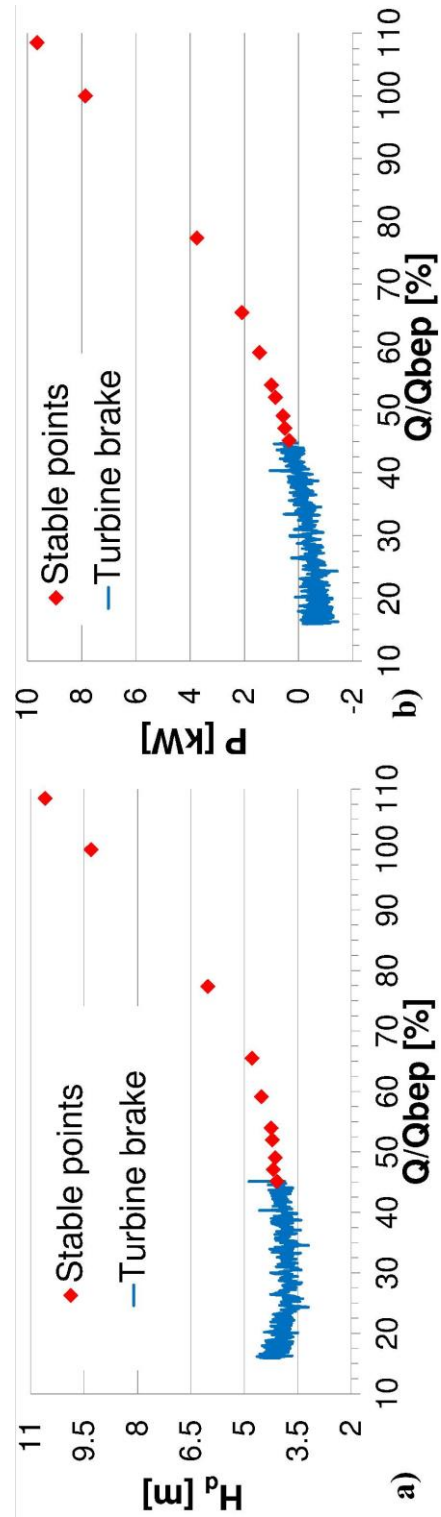
Fig. 27   Performance curve of the pump-turbine: a) head; b) mechanical power
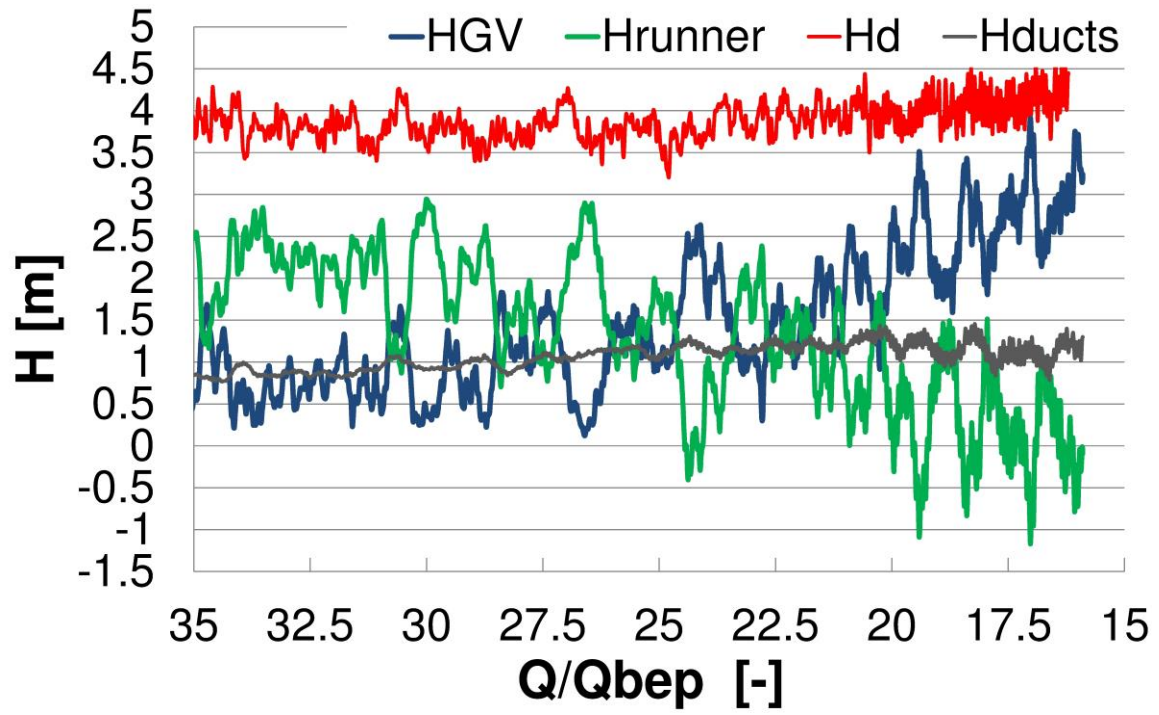
Fig. 28   Instantaneous mass flow averaged total pressure differences between
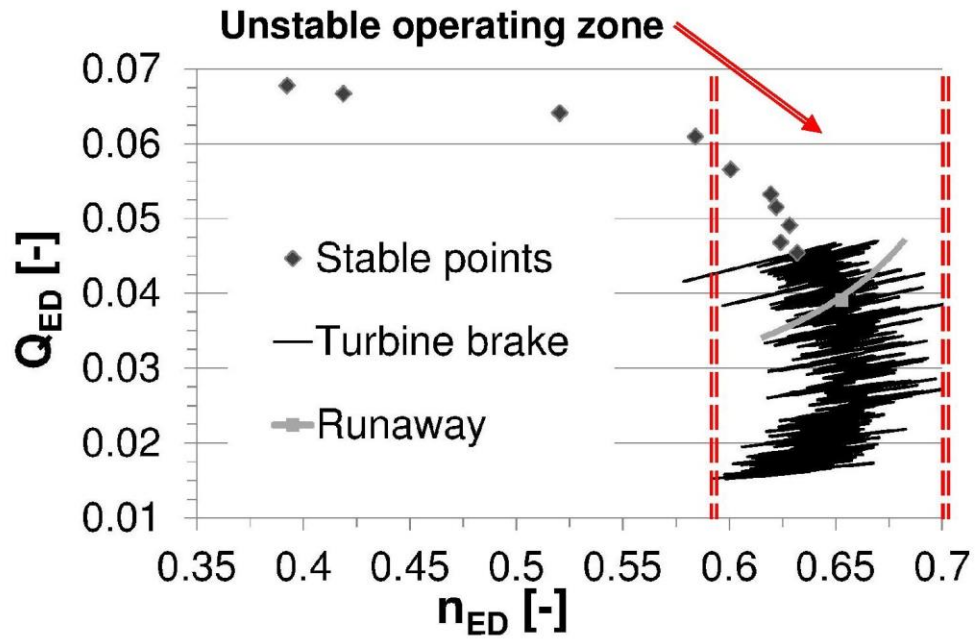
inlet and outlet of the different domains of the RPT.

Fig. 29   Numerical dimensionless discharge-speed curve

Runner

D$_2$ [mm]	B$_2$ [mm]	n$_b$	β$_{2c}$ [°]	φ$_{bep}$
400	40	7	26.5	0.125

Guide Vanes

D$_3$ [mm]	B$_3$ [mm]	n$_b$	α$_{3c}$ [°]	λ [°]
410	40	22	10÷30	-8÷8

Return channel

D$_4$ [mm]	B$_4$ [mm]	n$_b$	α$_{4c}$ [°]
516	40	11	30

Table 1 Pump-turbine data

	number of elements
Return channel	$5.11*10^6$
Guide Vanes	$3.55*10^6$
Runner	$3.74*10^6$
Draft tube	$3.22*10^5$
Leakage System	$3.47*10^5$
	$13.07*10^6$

Table 2 Mesh data